Graphitic Carbon Nitride (g-C_3N_4) and Its Modification as a Composite Material

Karel Klouda , Petra Roupcová * , Martina Vráblová , Kamil Maciej Górecki , Petra Bursíková , Romana Friedrichová , Kateřina Bátrlová , Eva Kuželová Koštálová , Zdeněk Starý , Jiří Tilhon

Posted Date: 7 February 2025

doi: 10.20944/preprints202502.0474.v1

Keywords: Graphitic carbon nitride; Doping of materials; melamine; polymer materials; degradation of pollutants

Article

Graphitic Carbon Nitride (g-C_3N_4) and Its Modification as a Composite Material

Karel Klouda [1,2], Petra Roupcová [1,*], Martina Vráblová [3], Kamil Maciej Górecki [3], Petra Bursíková [4], Romana Friedrichová [4], Kateřina Bátrlová [2], Eva Kuželová Košťáková [5], Zdeněk Starý [6] and Jiří Tilhon [2]

1 VSB – Technical University of Ostrava, Faculty of Safety Engineering
2 Occupational Safety Research Institute
3 Institute of Environmental Technology, VSB – Technical University of Ostrava
4 Technical Institute of Fire Protection, Ministry of the Interior – General Directorate of Fire Rescue Service of the Czech Republic
5 Technical University of Liberec
6 Institute of Macromolecular Chemistry, Czech Academy of Sciences
* Correspondence: petra.roupcova@vsb.cz

Abstract: This paper describes the preparation of g-C_3N_4 by polycondensation of melamine at 511 °C and its subsequent doping with Fe_2O_3, Cu, GO, rGO, DA and their combinations. Graphitic carbon nitride is a new material with plenty of applications e.g. in the fields of catalysis or water treatment. FTIR, thermogravimetric analysis was mainly used for identification and SEM images were taken at gradual resolution. The next part of the paper describes the preparation of composite compounds in polymer, PE-foil, PP-filaments for 3D printing, in PVB into nanofibers by electrostatic spinning. The aim of this article was to investigate the thermal stability of nanofibers prepared from PVB with g-C_3N_4 composite (18-20 %) by two methods: EL DC spinning and EL AC spinning. The material that exhibits the most effective synthesis will be subjected to further evaluation to assess its potential applicability in the photocatalytic degradation of pollutants.

Keywords: Graphitic carbon nitride; Doping of materials; melamine; polymer materials; degradation of pollutants

1. Introduction

It is a substance that is prepared by thermal polycondensation at a temperature of 450-660°C [1] from nitrogen-rich precursors with C-N core structure such as melamine, cyanamide, dicyandiamide, urea, thiourea; see scheme in Figure 1.

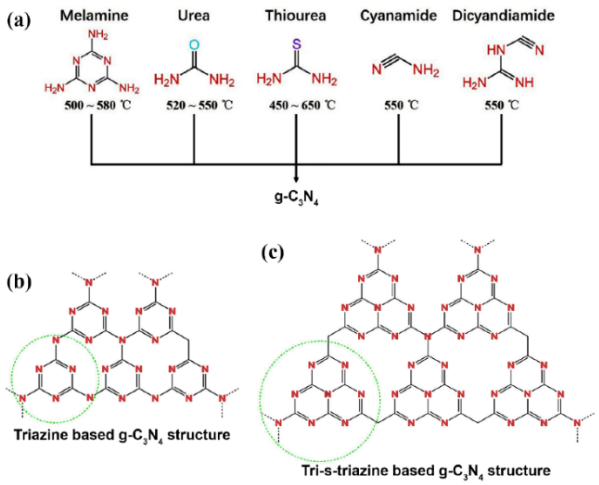

 doi:10.20944/preprints202502.0474.v1

Figure 1. Initial precursors of the synthesis process of g-C3N4, structures of nanosheets.

With a graphite-like layered structure, g-C_3N_4 is in a form of 2D nanosheets, based on s-triazine or tri-s-triazine (Figure 1) tectonic unit interconnected via tertiary amines [2]. The presence of sp^2-hybridized C and N results in the unique g-C_3N_4, which plays a prime role in photocatalytic technologies, it is a highly active non-metallic photocatalyst [3]. The photocatalytic activities of g-C_3N_4 are considerably affected by its structure, including its electronic structure. Both doping and composites are used for influence to obtain improved properties of new compounds, which then allow a wide range of possibilities for adaptive properties, e.g. for photocatalytic degradation, environmental remediation, removal of heavy metals from contaminated water, photocatalytic water splitting, photoreduction of CO_2, etc. Another factor is the influence of micro-, meso- and macro-pores in the fabric. Pore size influences water decomposition, production of H_2 and O_2, reduction of CO_2 (CH_3OH, CH_4). HARD-TEMPLATE METHOD, SOFT-TEMPLATE METHOD and TEMPLATE-FREE METHOD are also described. These methods modify the pore structure. g-C_3N_4 can be exfoliated chemically, mechanically and by ultrasound [4–6]. An important application of g-C_3N_4 is in wastewater treatment by photo-oxidation reactions, where organic pollutants are degraded, bacteria are inactivated, and toxic heavy metals, antibiotics and a range of organic compounds are removed by photo-reduction reactions [7–10]. One of the other applications of g-C_3N_4 is membrane formation, which is used to trap pollutants, phenols, pharmaceutical products, organic dyes, and for desalination. g-C_3N_4 shows good photocatalytic activity under visible light [11–13].

$gC,N + h\gamma \rightarrow C,N\ e^{-1} + O_2 \rightarrow {}^{\circ}O^{-}2$

$gC,N\ e^{-1} + H_2O \rightarrow {}^{\circ}{}^{\circ}OH$

$^{\circ}{}^{\circ}OH/{}^{\circ}O^{-}{}_2$ + Pollutant → Degradation

Graphitic carbon nitride can be functionalized [14] − COOH, − SO_3H, − OH to affect the electrochemical and physicochemical properties by elemental doping, both non-metallic (S, O, B, Cl, F) and metallic (Fe, Ni, Pb, Ag, Au). Applications in supercapacitors, in photocatalytic water splitting, as a flame retardant, appear to be promising [15,16]. g-C_3N_4 is one of the photocatalysts with minimal toxicity, a chemically stable substance with efficient light absorption in the visible near-infrared region [17,18].

The aim of this article was to synthesize gC3N4 and its modifications with diverse materials and to implement these modifications within a composite framework with polymer materials. The synthesized products were subsequently subjected to FT-IR, SEM, and TGA analyses to facilitate comparative evaluation and further examination of their photocatalytic properties.

2. Materials and Methods

2.1. Materials

Chemicals:

- Melamine – purity 99 %; CAS: 108-78-1; Sigma-Aldrich s.r.o.;
- Low Density Polyethylene (LDPE) TYPE 100 BW Exxon Mobil;
- Polyvinyl butyral (PVB), Mowital, Kuraray Europe GmnH; Germany;
- Dopamine hydrochloride – PA; CAS: 62-31-7; Sigma-Aldrich s.r.o.;
- Tris (hydroxymethyl) amino- methane; purity 99,8 %; Sigma-Aldrich s.r.o.; CAS: 77-86-1;
- Iron oxide - nanoscale –purity 96 %; CAS:1309-37-1; Sigma-Aldrich s.r.o.;
- Graphene oxide (GO)– preparation by Hummers' method [19];
- Reduced graphene oxide (rGO) – reduced by ascorbic acid [19];
- Graphene oxide MEND (GO MEND) – provided by the Mendel University in Brno in suspension 2gL^{-1} [20];

2.2. Methods

- **FTIR spectroscopy** (Nicolet iS20 FTIR Spectrometer: type of experiment: single reflection diamond ATR; sample preparation: solid samples measured directly, powdered samples ground into a fine powder; the spectra were not modified using any corrections; measurement

 doi:10.20944/preprints202502.0474.v1

conditions: the spectral resolution: 4 cm^{-1}; the number of scans: 128; technical parameters of the device:

-detector: thermoelectrically cooled DTGS

-IR source: single-point IR ceramic

-laser: solid-state, temperature-controlled diode laser

-beamsplitter: KBr

-Spectral range: 7800 – 350 cm^{-1}

-Omnic 9 software

- **SEM EDX spectroscopy: (**Tescan Vega 4, Tescan Vega 3) with accelerating voltage was 15 ke.
- **Thermogravimetric analysis (**STA 449 F3 JUPITER DTA): air atmosphere, flow rate is 40 ml/min, temperature range is from 30 °C to 750 °C, speed heating is 20 °C/min.
- Other instruments:

-Electric furnace 018LP fg Svoboda

-Mini extruder Mini CTW Haace

-Hydraulic press FONTIJNE.

2.3. Preparation of g-C_3N_4

It is prepared by thermal polycondensation of melamine. The melamine powder was poured onto an aluminum foil bed and then placed in an electric furnace. The rise to the reaction temperature of 511°C from 19°C took one hour. Polycondensation at this temperature lasted for 4 hours. The furnace cooled down for about 2 hours after switching off and 4.12 g of the yellow product of g-C_3N_4 was obtained (20% yield).

2.4. Subsequent Reactions of g-C_3N_4

a) Reactions with dopamine hydrochloride

g-C_3N_4 (2.8 g) + 30 ml of 50% C_2H_5OH was alternately mixed and sonicated for about 30 minutes. Subsequently, a solution of DA·HCl (1.4 g) in 30 ml of distilled water with 30% H_20_3 (15 ml) was added and modified in TRIS to pH 8.5. The reaction mixture was mixed at laboratory temperature for 16 hours and then filtered and dried at a temperature of 55 °C. (point a)

b) Reaction with graphene oxide (GO)

Together in aqueous medium, the mixture of g-C_3N_4 (1.1 g) with GO (1.0 g) was alternately mixed and sonicated for 16 hours, then the mixture was filtered and dried at a temperature of 55 °C.

c) Reaction with reduced graphene oxide rGO

This reaction followed the same reaction pathway as in point a)

d) Reaction with iron nano-oxide without and after addition of GO

g-C_3N_4	(3.85 g)	30 ml $C_2H_5OH_8$	C_3N_4 (3.85 g) 30 ml C_2H_5OH
Fe_2O_3	(1 g)		Fe_2O_3 (1 g)
			GO (2 g) 15 ml C_2H_5OH

e) Reaction with iron nano-oxide after addition of (DA) dopamine hydrochloride

g-C_3N_4	30 ml $C_2H_5OH_8$
Fe_2O_3 (5,39 g)	mixed and sonicated for 30 minutes
DA·HCl (1.4 g)	40 ml H_2O + 15 ml H_2O3 (50%)
TRIS pH 8.5	

It was mixed at laboratory temperature for 16 hours and then the reaction mixture was filtered and dried at a temperature of 55 °C.

Mixtures of g-C_3N_4 with ethanol were magnetically mixed side by side in Erlenmeyer flasks for 15 minutes; without mixing they were placed in a sonication bath. This run for 1 hour and graphene oxide was added to the second flask. The sonication bath was heated to 40-50 °C. The alternating procedure of mixing and sonication took 2 hours. Both reactions were then mixed at a temperature of 21 °C overnight (16 hours). Filtration followed, the cake was washed with C_2H_5OH and distilled water and then the filter cake was allowed to dry at a temperature of 55 °C.

f) Thermal reaction with graphene oxide in the presence of hydrogen peroxide

 doi:10.20944/preprints202502.0474.v1

Together in aqueous medium (20 ml of H_2O), the mixture of g-C_3N_4 (1.0 g) with GO (1.0 g) was alternately mixed and sonicated for 1 hour. Subsequently, the reaction flask containing this mixture was placed in a water bath (70-80°C) and hydrogen peroxide (30%) was added in an amount of 35 ml and the flask was closed with a plastic stopper. The flask was left in this water bath for 2 hours. The contents of the flask were then filtered and the filtered product was dried.

g) Reactions with graphene oxide provided by the Mendel University in Brno (GO-MEND)

g-C_3N_4 (1 g) + 7 ml of C_2H_5OH sonicated for 30 minutes, then 12 ml of GO suspension were added. Alternately mixed (shaken) and sonicated (40-50 °C) for 2 hours (the mixture was grey in colour). Subsequently, the suspension was poured onto PVDF with one side laminated with PP. PVDF was a non-woven fabric prepared by electrospinning. The plastic sample was spherical in shape and was placed in Petri dish. The rest of the suspension was poured onto conventional filter paper and then the suspension was spontaneously evaporated. The suspension on the plastic substrate was placed in a 50 °C oven. The next day – the result was not a film as when the aqueous GO-MEND suspension itself was dried. The result was a grey-yellow powder (Figure 3) that did not adhere to the substrate, either on the plastic, nanofibers or filter paper. When the weight-to-weight ratio of g-C_3N_4 to GO was reduced (0.004 g, 0.004 g of GO-MEND in 2 ml of suspension), a cracked film was obtained, but it adhered to the polymer substrate, see Figure 4.

h) Presence of nano iron oxide in the melting of melamine

The polycondensation of melamine was repeated with weights of about 20 g of melamine with approximately 20% yield of C_3N_4. The melting process was carried out in the presence of 10% nano iron oxide relative to melamine. After one hour, a temperature of 511 °C was reached and the reaction was held at this temperature for 2.5 hours. After opening the furnace, no common substance of g-C_3N_4 was found as it was repeatedly found in polycondensation of melamine itself; only a red-brown powder was found. Its weight corresponded in essence to the initial weight of Fe_2O_3.

The experiment was repeated with weights of 25.26 g of melamine with 1.75 Fe_2O_3, i.e. 7% relative to melamine. Temperature and time remained the same. The result was also the same - Fe_2O_3 powder in essence with the initial weight of approximately 1.66 g.

i) Presence of graphene oxide in the melting of melamine

The melting process was carried out – polycondensation of melamine together with GO, weights: melamine 26.3 g, GO 1.0 g. The mixture was mixed and placed in a furnace at 511°C for one hour until the specified temperature was reached, and then the temperature was held for 2.5 hours. After opening the furnace, some blackening of the furnace with carbon black was found; despite this finding, samples were taken for FTIR analysis and SEM acquisition.

j) Reaction with DA in the presence of Cu2+ and Fe

g-C_3N_4 (2.6 g) was sonicated in 25 ml of distilled water for 0.5 hour, then the reaction flask was magnetically mixed with Fe-screw and an aqueous solution of 6.02 g $CuSO_4 \cdot 7H_2O$ in 30 ml H_2O was added. The prepared mixture was mixed for 0.5 hour and then a solution of 3.02 g dopamine hydrochloride in 25 ml H_2O with TRIS and 5.5 ml H_2O_2 was added. Upon addition of dopamine, the reaction mixture turned brown and spontaneously heated to approximately 80 °C. The flask with this reaction mixture was mixed for 1 hour and then left at room temperature overnight. The solid product was filtered and dried. The filtrate obtained was a brown-black product with a weight of 2.8 g.

k) Reaction with $CuSO_4 \cdot 5H_2O$ (Cu^{2+}) and Fe (VRUT) solution

The procedure was similar to that in point h) except for the part of the reaction where dopamine hydrochloride solution was added.

2.5. Preparation and Identification of Polymer Composites Film with Polyethylene (g-C_3N_4, g-C_3N_4-PDA)

Low density polyethylene (LDPE) was used as the matrix for the preparation of the composite. The composite containing 10 wt% g-C_3N_4 (or 10 wt% g-C_3N_4-PDA) was prepared by mixing in melt on a mini-extruder. Mixing was carried out at a temperature of 190 °C and a screw speed of 60 min^{-1} for one minute. The composite material thus obtained was subsequently transferred to a Fontijne hydraulic press, where 0.5 mm thick films were pressed at a temperature of 190 °C.

 doi:10.20944/preprints202502.0474.v1

2.6. Preparation of Filaments and Their Application in 3D Printing – To Be Added

The composite material for the preparation of the printing filaments was prepared by mixing in melt using a Brabender Plasticorder W50 EH mixer at 190 °C with a rotor speed of 60 rpm. The mixing time was 8 minutes. The polypropylene homopolymer (PP) Moplen HP501L (LyondellBasell) was used as the matrix for the preparation of the composite. The content of g-C_3N_4 in the composite was 10 wt%. After granulation, the material was extruded at a temperature of 190 °C through a capillary nozzle with a diameter of 1.6 mm and aspect ratio L/D=12. The resulting printing filament had a diameter of 1.7 mm, see Figure 2.

Figure 2. PP-gC_3N_4 filament samples**.**

2.7. Nanofibers Prepared by DC and AC Electrospinning

Electrospinning is currently considered to be the simplest technology for producing fibers with precisely defined properties [21], which uses a solution or melt and which is simultaneously based on and uses an electrostatic field during production. [22,23]. Fiber formation using a combination of electrostatic field and other forces is the goal of modern efforts to increase the range of electrospinning manufacturing options. Examples of this include the use of low frequencies [24], high frequencies [25] or air blowing [26]. However, another study [27] has shown that a static direct current (DC) high voltage source can be replaced by dynamic AC power, with significant productivity gains. The differences between the different approaches to the use of AC or DC electrospinning can be summarised as follows: The use of a dynamic AC voltage leads to a several-fold increase in productivity (using the same device) compared to DC voltage in the case of multiple fluid streams that are ejected from a continuously charged and discharged droplet – thus the AC being more permeable [27,28]. Operation without collector. The motion of the flying nanofibre plough produced by AC voltage electrospinning is not affected by the ground potential but by the electric field surrounding the spinneret. This means that it is not necessary to have a grounded collector. When producing fibers in a confined environment (e.g., pharmaceutical manufacturing), collection is more efficient if the problem of fiber stickiness that occurs with DCES on grounded surfaces (i.e., almost all surfaces except the charged spinneret) is eliminated [29].Fibre production. Fiber materials are key ingredients for other high-value three-dimensional applications such as tissue engineering or composites. However, their fabrication using the commonly used DCES method is difficult due to the occurrence of repulsion between the flying fibers [30]. In contrast, using AC electrospinning, twisted yarns can be easily produced without complex collection problems [27,31,32].

Various factors affecting the process. In addition to the key factors that affect DCES (e.g. polymer concentration, electric field strength, etc.), there are other possibilities such as adjusting the frequency and shape of the AC voltage waveform. These changes could be used to optimize the ACES process, for example, in terms of productivity or morphology of the resulting fibers [29].

 doi:10.20944/preprints202502.0474.v1

A paper has been published [33] where g-C_3N_4 was incorporated by electrospinning into PVDF fibers in order to prepare a membrane for use in the photocatalytic degradation of pollutants (the experiment was executed on Rhodaamine B) and subsequently another experiment has been published by essentially the same authors [20], where C_3N_4 was doped into fibers with graphene oxide in a similar manner as described in this publication. Introduction of gC_3N_4 as a composite into PVB nanofibers by electrospinning was done at TUL.

a) DC electrospinning - Nanospider™ (Elmarco, CZ)

Sample 1.0, see Figure 33, control sample – polyvinyl butyral (PVB, B60H, Kuraray), 10 wt% PVB solution in ethanol. Electrospinning - Nanospider™ – electric voltage on spinning electrode +30 kV; electric voltage on collector -10 kV; electrode spacing 200 mm; diameter of the dosing device 0.7 mm; travel speed of the dosing device 1 sec/50 cm; relative humidity 40%; temperature 22°C; substrate material - spunbond-type non-woven fabric 30 g/m² (PFNonwovens, CZ); substrate material removal rate 20 mm/min.

Sample 1.1, see Figure 34, - 10 wt% PVB in ethanol with the addition of 20 wt% g-C_3N_4 from dry matter of the polymer. The final theoretical concentration is 16.67 wt% gC_3N_4 from dry matter of the resulting fibers. The formation of the solution was in the following procedure: weighing a quantity of ethanol, adding g-C_3N_4 powder crushed into smaller particles in a mortar grinder, sonication by ultrasonic homogenizer 5x10 sec; adding PVB, mixing on a magnetic mixer for 8 hours. Electrospinning - Nanospider™ – electric voltage on spinning electrode +30 kV; electric voltage on collector -10 kV; electrode spacing 200 mm; diameter of the dosing device 0.7 mm; travel speed of the dosing device 1 sec/50 cm; relative humidity 40%; temperature 22°C; substrate material - spunbond-type non-woven fabric 30 gm $^{-2}$ (PFNonwovens, CZ), see Figure 35; substrate material removal rate 20 mm/min.

b) AC electrospinning – rod electrode (TUL)

Sample 2.1, see Figure 36 – AC electrospinning was carried out on equipment developed by the TUL FP and FS team. The spinning process took place under the following conditions: Effective voltage Uef 35 kV; sine wave signal; frequency 50 Hz; distance of the black paper (electrically inactive collector) from the rod spinning electrode 350 mm; relative humidity 40%; temperature 22°C.

3. Result and Discussion

3.1. gC_3N_4 with Dopants

3.1.1. FT-IR Analysis

Most of the experiments were focused on the doping of g-C_3N_4, mostly at laboratory temperature (mean value 21°C). Iron oxide powder in microscale, GO (FTIR presented in Figure 5), rGO (FTIR presented in Figure 4), copper in the native state obtained according to the principle of electrochemical series of metals, Beketov's series, i.e. copper salt and Fe-VRUT (FTIR presented in Figure 7) were used as doping agents. In some experiments, dopamine hydrochloride was used, which was polymerized in the reaction to polydopamine, which has adhesive abilities and the formed layer has catechol and amino functional groups on the surface.

Slightly increased reaction temperature was used during the reaction of GO in a hydrogen peroxide environment; this was to modify GO to so-called holey graphene oxide (HGO) during the reaction of g-C3N_4 (FTIR presented in Figure 6)

FTIR analysis was carried out on selected products of the g-C_3N_4 reaction and SEM images were taken at different resolutions of 500 μm, 50 μm and 5 μm. Thermal analysis was carried out and evaluated on the products from reaction 1.3.d.

All acquired spectra are characterized by two regions, namely at 2800 cm^{-1} and then a forest of peaks in the range 1600-500 cm^{-1}, where there are vibrations of CN – heterocycles. A more detailed description of the spectra is given under Figure 3. In all prepared products, a wavenumber of 808 cm^{-1} is identified, which is interpreted as a triazine ring vibration in accordance with the reference [33].

 doi:10.20944/preprints202502.0474.v1

For the products with GO, the FTIR shows a characteristic peak C=O 1637 cm^{-1}.

FTIR analysis was carried out for the initial graphitic carbon g-C_3N_4 to determine the characteristic bands and these were compared with the bands of g-C_3N_4 + Fe_2O_3 and g-C_3N_4 +Fe_2O_3 + GO (Figure 3).

In addition to the main preparation of g-C_3N_4, the melting of melamine in an electric furnace was tested together with Fe_2O_3 and with GO at the same temperature. In the case of melting with Fe_2O_3, the reaction found in thermal analysis was confirmed, where g-C_3N_4 decomposes in the presence of Fe_2O_3. In the case of GO, the melting temperature is approximately identical to the temperature at which the second exothermic effect takes place for GO. The obtained product visually resembles a mixture of carbon black and C_3N_4 and identification by FTIR, see Figure 8.

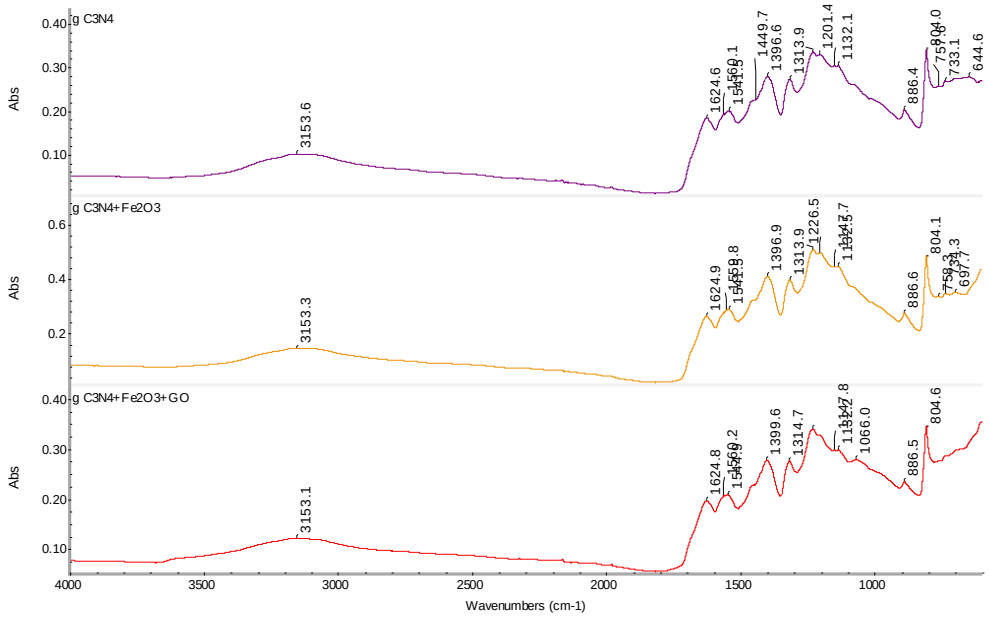

Figure 3. Comparison of FTIR spectra of g-C_3N_4, g-C_3N_4 + Fe_2O_3 and g-C_3N_4 + Fe_2O_3 + GO samples with determination of characteristic bands.

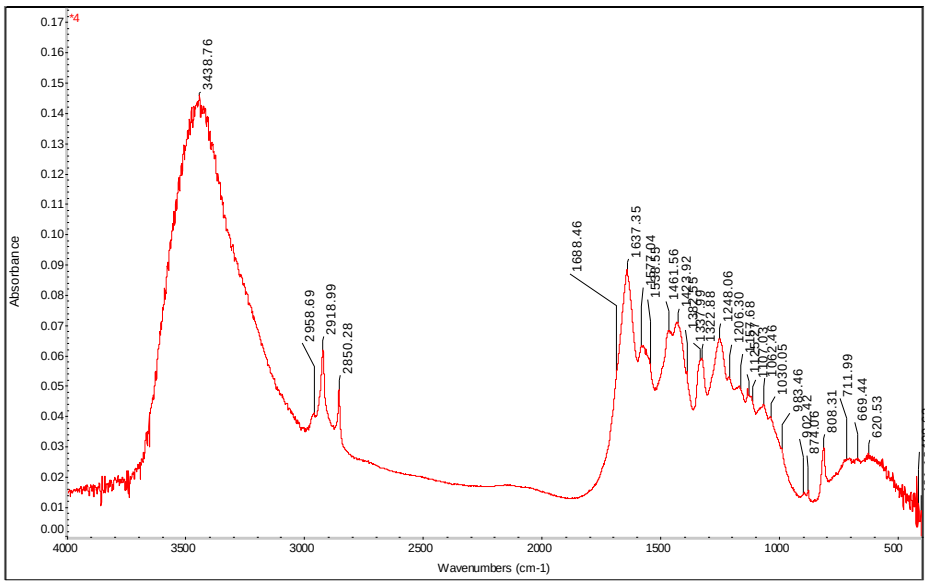

Figure 4. FTIR of g-C_3N_4 + rGO.

 doi:10.20944/preprints202502.0474.v1

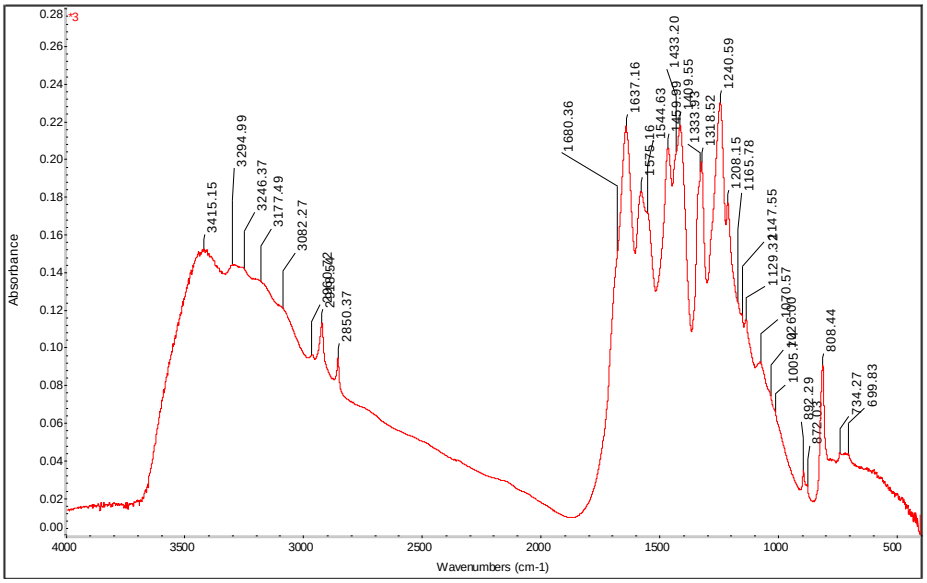

Figure 5. FTIR of g-C_3N_4 + GO.

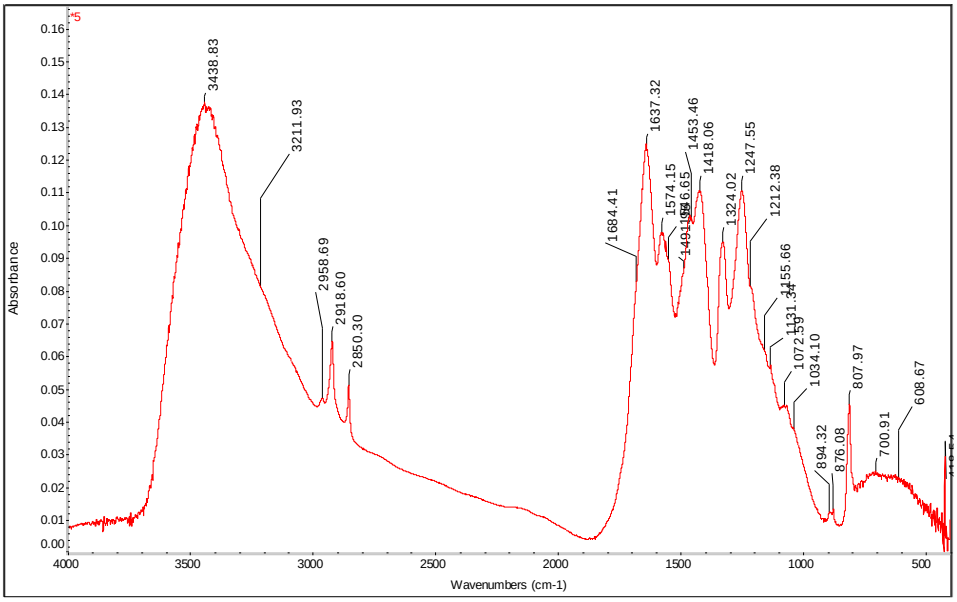

Figure 6. FTIR of g-C_3N_4 + GO + 30% H_2O_2.

Preprints.org (www.preprints.org) | NOT PEER-REVIEWED | Posted: 7 February 2025 doi:10.20944/preprints202502.0474.v1

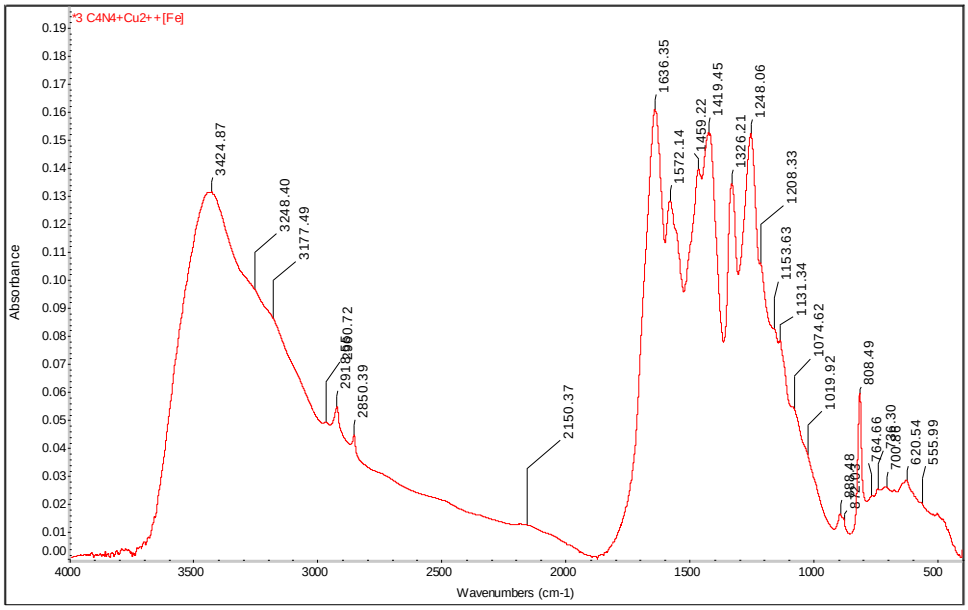

Figure 7. FTIR of C_3N_4 + Cu^{2+}[Fe].

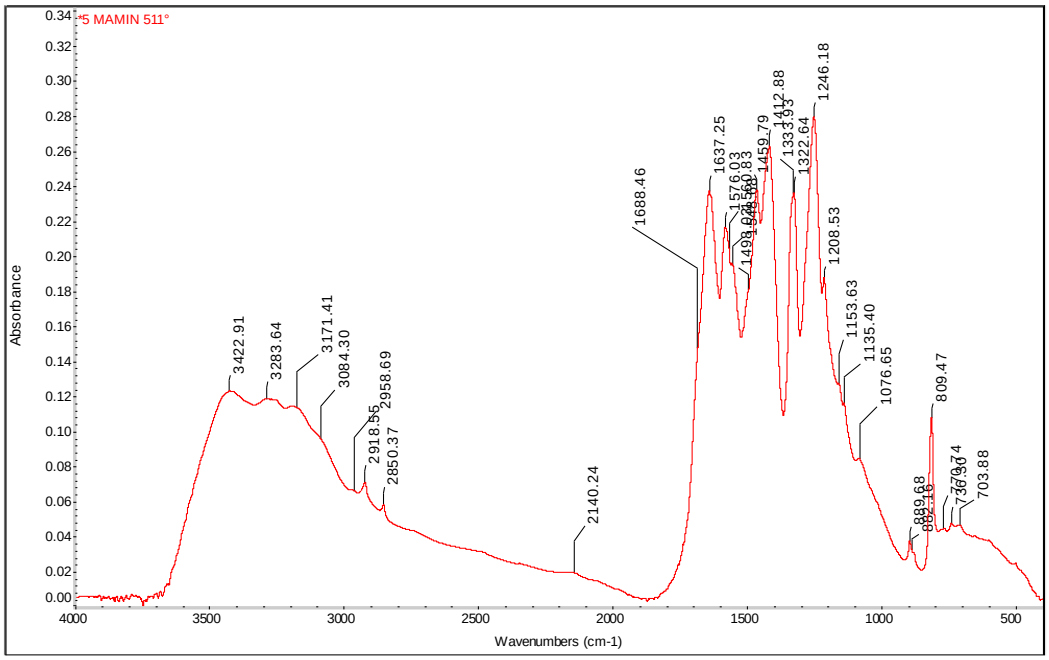

Figure 8. FTIR of melamine 511°C -GO.

The spectra show characteristic bands that are practically the same for all measured samples. Based on the triazine-based structure, we can conclude that we are looking for C-N, C=N, CN cycle vibrations and probably also NH_2.

wide band 3600 – 2700 cm^{-1}	vibration NH_2
1625 - 1540 cm^{-1}	vibration C=N
1460 - 1200 cm^{-1}	vibration C-N
1148 and 1132 cm^{-1}	vibration CNC
805 cm^{-1}	vibration of CN cycle

3.1.2. SEM Analysis

The microstructure of sample gC_3N_4 is presented in Figure 9. The lowest magnification (A) shows occurrence of aggregates randomly distributed at the observed surface. The higher magnification (B) shows that the aggregates are formed by the particles of different size and shape of

 doi:10.20944/preprints202502.0474.v1

porous structure. The closer analysis (C) reveals occurrence of plate-like particles (from approx. 1 μm to 5 μm) surrounded by the smaller, irregular, closely packed crystals.

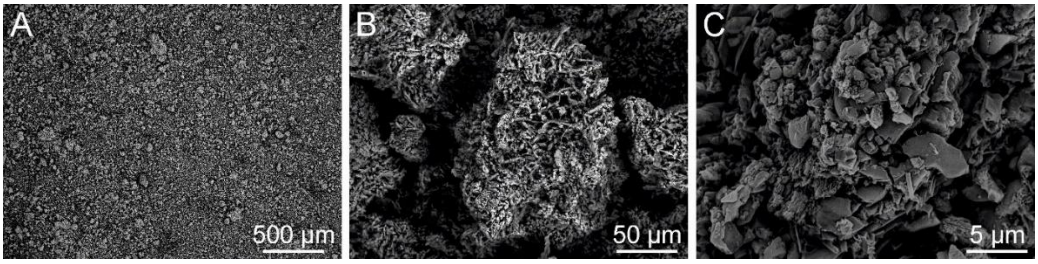

A – the size of a scale bar 500 μm B – 50 μm C – 5 μm

Figure 9. SEM micrographs of g-C_3N_4, SEM: SE+BSE.

The microstructure of g-C_3N_4 + Fe_2O_3 is presented in Figure 10. The images (A) and (B) reveal the occurrence of the aggregates that show visible porous, sponge-like surface. The higher magnification shows that the aggregates are composed of bigger, rounded plates (approx. 6 μm, the grey structures). The visible white sphere-like components are connected to the Fe_2O_3. The spheres partially cover the g-C_3N_4 surface forming the aggregates of different size up to 500 nm. The size of the single sphere-like particle is approx. 200 nm.

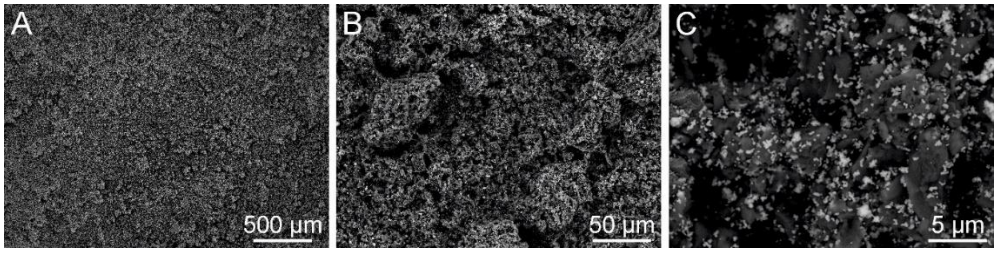

A – the size of a scale bar 500 μm B – 50 μm C – 5 μm

Figure 10. SEM analysis of g-C_3N_4 + Fe_2O_3, SEM: SE+BSE (Tescan Vega 4).

The microstructure of sample g-C_3N_4 + Fe_2O_3 + GO is presented in Figure 11. The surface of sample resembles the structure observed for the g-C_3N_4 (Figure A). The micrographs (A) and (B) show visible porous materials composed of plates with defined sharp edges (C). The estimated size of plates is in a range of 6 – 7 μm. In comparison to sample g-C_3N_4, the plates observed for g-C_3N_4 + Fe_2O_3 + GO are not surrounded by smaller stacked crystals. The visible white sphere-like structures (Fe_2O_3) are similar like for sample g-C_3N_4 + Fe_2O_3 (Figure 10). However, the observed aggregates of spheres are visibly larger, up to 2 μm.

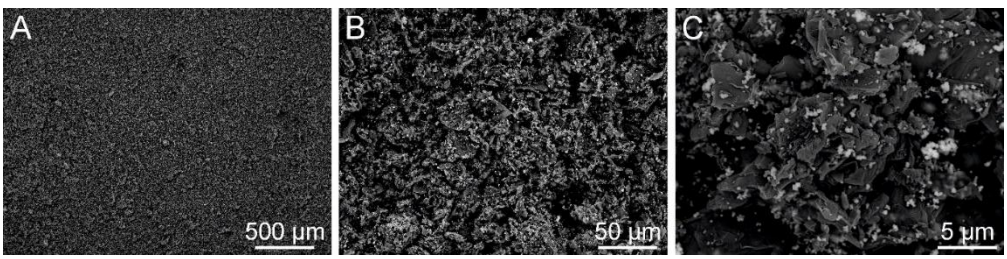

A – the size of a scale bar 500 μm B – 50 μm C – 5 μm

Figure 11. SEM analysis of g-C_3N_4 + Fe_2O_3 + GO, SEM: SE+BSE(Tescan Vega 4).

The microstructure of g-C_3N_4 + rGO is presented in Figure 12. The micrographs (A) and (B) show formation of aggregates of porous structures. The highest magnification (C) shows that the aggregates are composed of crystals of different size and shape. The bigger, coarse particles of size

 doi:10.20944/preprints202502.0474.v1

approx. 8 μm are surrounded by smaller plate-like particles stacked and closely packed in layers. The micrographs reveal also occurrence of elongated tube-like crystals of length approx. 5 μm

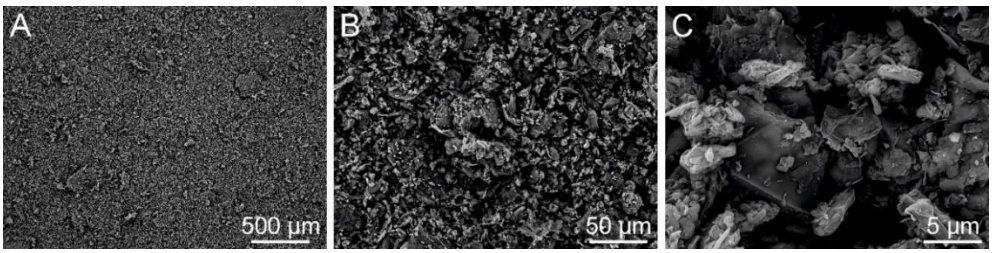

A – the size of a scale bar 500 μm B – 50 μm C – 5 μm

Figure 12. SEM analysis of g-C_3N_4 + rGO, SEM: SE+BSE (Tescan Vega 4).

The microstructure of g-C_3N_4 + GO is presented in Figure 13. The micrographs show occurrence of big aggregates (A) that at higher magnification (B) resembles the tree bark. The image shows formation of the 'base' structures – big solid particles, covered by smaller structures of undefined shape and of visibly higher porosity. The size of 'base' particles (C) is estimated to approx. 21 – 22 μm, while the smaller 'covering' particle size (C) is approx. 2.5 - 3 μm.

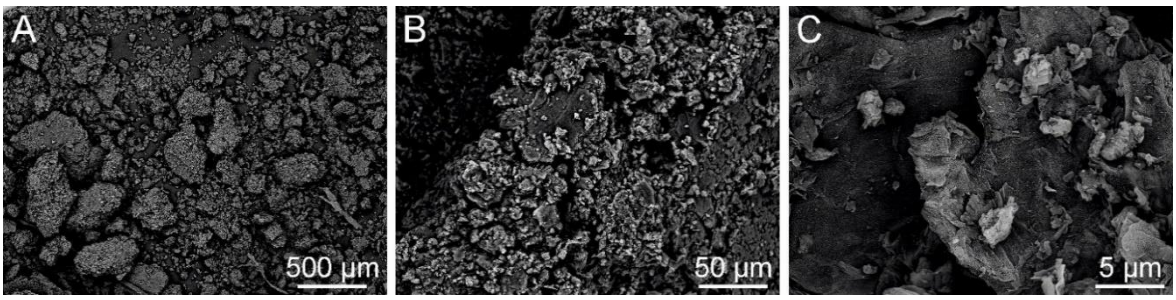

A – the size of a scale bar 500 μm B – 50 μm C – 5 μm

Figure 13. SEM analysis of g-C_3N_4 + GO, SEM: SE+BSE (Tescan Vega 4).

The microstructure of g-C_3N_4 + GO + 30% H_2O_2 is shown in Figure 14. The analysis of micrographs (A) and (B) shows formation of aggregates of different size. The particles observed at higher magnifications do not resemble the structures observed for previously described materials. The shape of particles is hard to define – some of the structures resemble a round-edged, deformed blocks, while other particles seem to be composed of closely packed, rounded plates. The estimated shape of particles is approx. 2 – 5 μm.

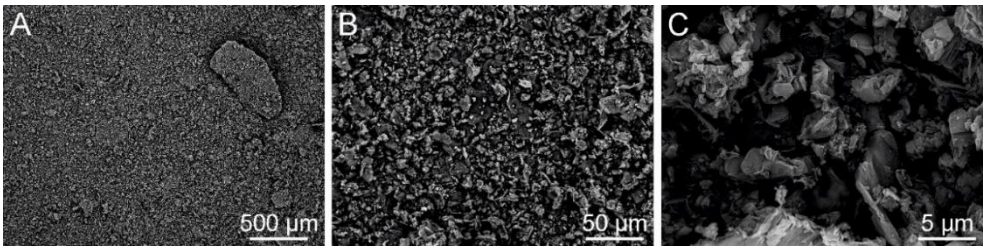

A – the size of a scale bar 500 μm B – 50 μm C – 5 μm

Figure 14. SEM analysis of g-C_3N_4 + GO + 30% H_2O_2, SEM: SE+BSE (Tescan Vega 4).

The microstructure of C_3N_4 + Cu_2+[Fe] is presented in Figure 15. The micrographs (A) and (B) show formation of aggregates of different shape and size. The lighter particles composed of sphere-like crystals are most probably related to Fe. The highest magnification (C) allows to observe the formation of needle-like aggregates, characteristic for CuO. The micrographs do not show occurrence of plates, either rounded or sharp. The irregular blocks of size approx. 12 μm are covered by smaller

 doi:10.20944/preprints202502.0474.v1

formations. The estimated size of Fe related particles is approx. 500 nm (single sphere), while the aggregates of Fe are up to 4 – 5 μm. The length of CuO needles is approx. 500 nm.

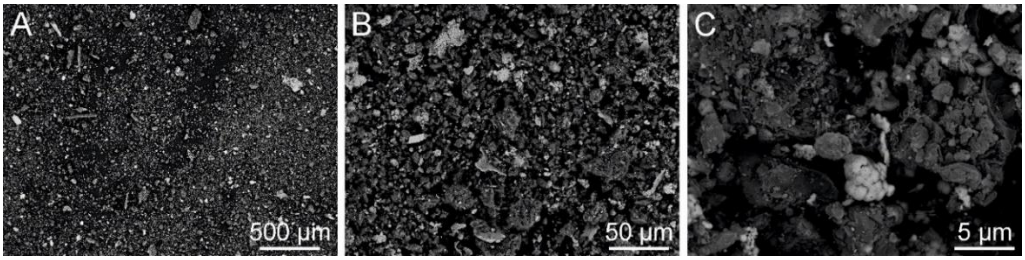

A – the size of a scale bar 500 μm B – 50 μm C – 5 μm

Figure 15. SEM analysis of g-C_3N_4 + Cu^{2+}[Fe], SEM: SE+BSE (Tescan Vega 4) .

The microstructure of melamine 511°C - GO is presented in Figure 16. The micrographs (A) and (B) show the sponge-like structure with visible porosity. The highest magnification (C) shows the solid particle composed of several closely stacked layers. The determination of size of individual plates/layers is impossible.

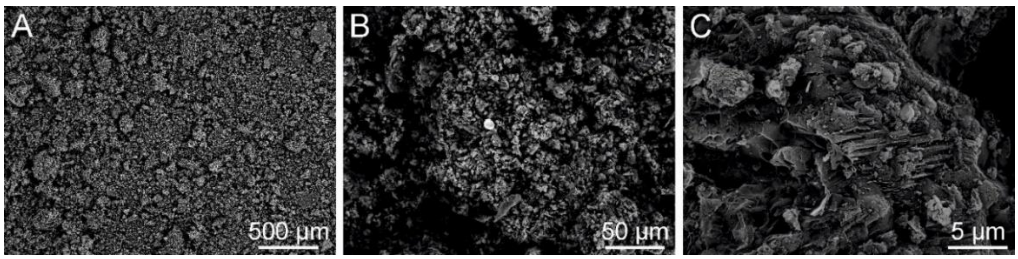

A – the size of a scale bar 500 μm B – 50 μm C – 5 μm

Figure 16. SEM analysis of melamine 511°C - GO, SEM: SE+BSE (Tescan Vega 4)**.**

3.1.3. TGA Analysis

The result of thermogravimetric analysis of these products compared to the initial g-C_3N_4 was interesting. This showed the exothermic effect associated with the decomposition of the C_3N_4 molecule in the presence of Fe_2O_3 at temperatures around 600°C (Figure 17 and 18). The carbon nitride itself is in essence stable at this temperature, decomposing with endothermic effect, weight units in %, Figure 19. In addition to the main preparation of g-C_3N_4, the melting of melamine in an electric furnace was tested together with Fe_2O_3 and with GO at the same temperature. In the case of melting with Fe_2O_3, the reaction found in thermal analysis was confirmed, where g-C_3N_4 decomposes in the presence of Fe_2O_3. In the case of GO, the melting temperature is approximately identical to the temperature at which the second exothermic effect takes place for GO. The comparison of the thermal properties of g-C_3N_4, g-C_3N_4 + Fe_2O_3, and g-C_3N_4 + Fe_2O_3 + GO revealed differences in mass losses and thermal transitions of the individual samples. In the thermogravimetric analysis of pure g-C_3N_4, an endothermic peak was observed at 108.3 °C, associated with a mass loss of -1.93%, likely caused by the release of water or other volatile substances. The main exothermic decomposition occurred with a mass loss of -75.28%, and the residual mass at 750.1 °C was 22.44%.

The addition of Fe_2O_3 caused a shift in the endothermic peak to 106.5 °C, with a slightly reduced initial mass loss of -1.83%. A significant exothermic peak was observed at 596.3 °C, accompanied by a mass loss of -76.47%. The residual mass was also lower (21.64% at 749.3 °C), which can be attributed to the oxidation of residual carbon species catalysed by Fe_2O_3.

The addition of graphene oxide (GO) led to further significant changes. The endothermic peak shifted to a lower temperature (76.4 °C), with the initial mass loss being the smallest (-1.38%). A new exothermic event was observed at 238.9 °C, associated with an additional mass loss of -7.08%, likely due to the decomposition of oxygen-containing functional groups in GO (epoxy, hydroxyl, carbonyl,

 doi:10.20944/preprints202502.0474.v1

and carboxyl groups). The main exothermic peak shifted to 599.1 °C, with a total mass loss of -68.94%, and the residual mass reached its lowest value (20.91% at 749.2 °C). The total exothermic energy of the mixture increased to 5383 J/g, indicating higher reactivity.

The presence of GO introduced a more complex thermal decomposition pathway, as evidenced by an intermediate step in the mass loss and a lower residual mass.

Overall, the comparison demonstrated that the composition of g-C_3N_4 + Fe_2O_3 + GO exhibits the most complex decomposition and thermal response. The presence of Fe_2O_3 caused a significant exothermic peak, while the addition of GO resulted in a multiphase decomposition and increased exothermic energy. The lower residual mass in the GO-containing mixture confirms greater degradation of the organic component, likely due to interactions between GO and the other components. The results clearly indicate that the addition of GO and Fe_2O_3 alters the thermal behaviour of the entire system and enhances its reactivity.

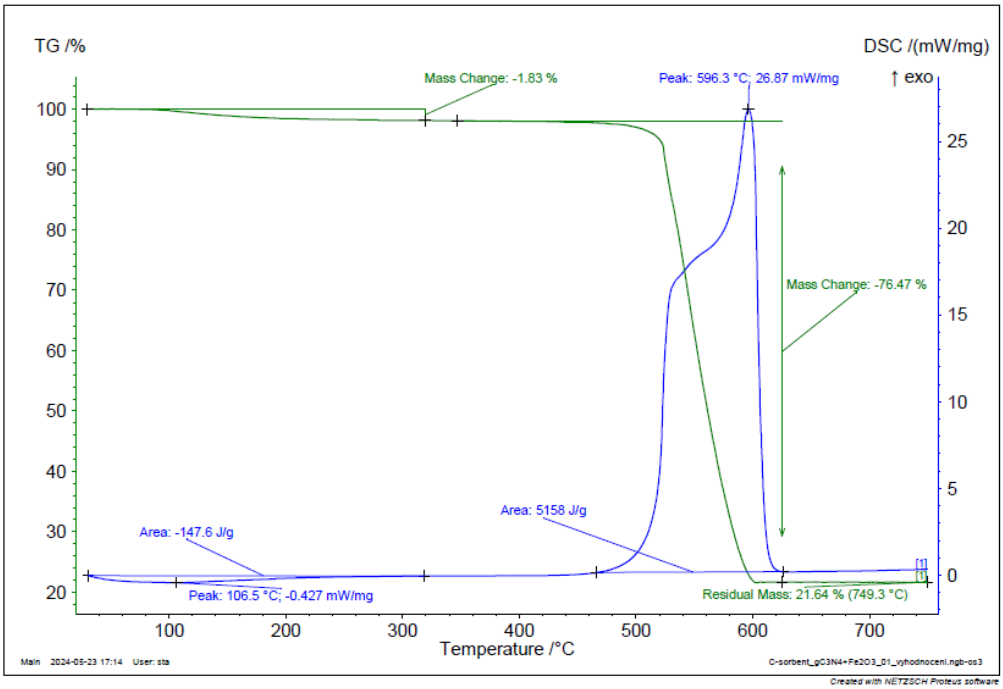

Figure 17. TGA and DSC analysis of g-C_3N_4 + Fe_2O_3.

 doi:10.20944/preprints202502.0474.v1

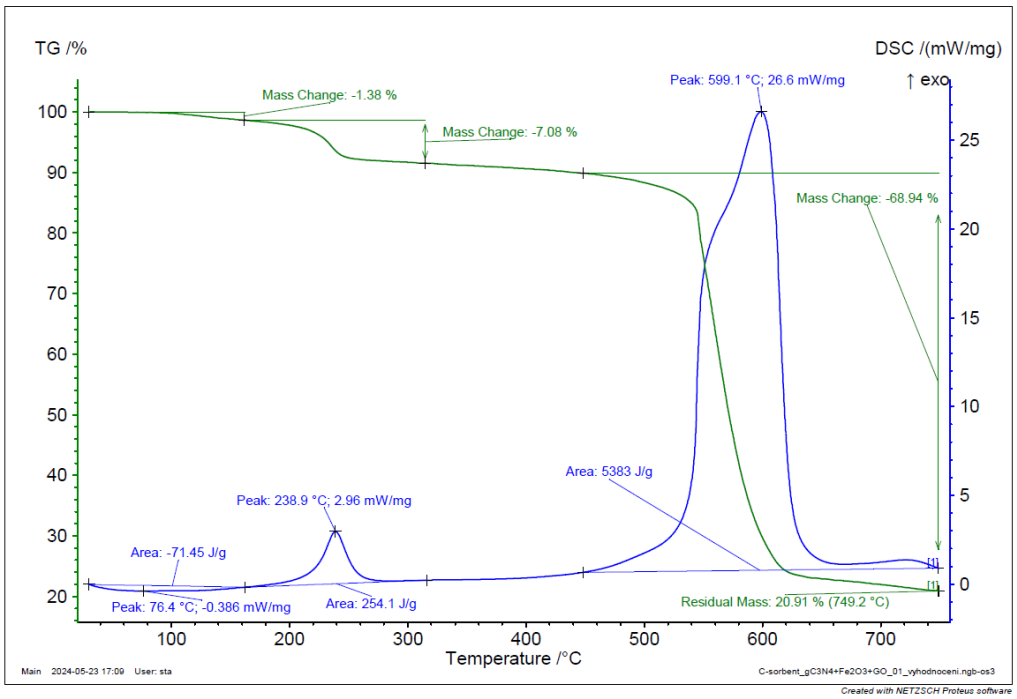

Figure 18. TGA and DSC analysis of g-C_3N_4 + Fe_2O_3 + GO.

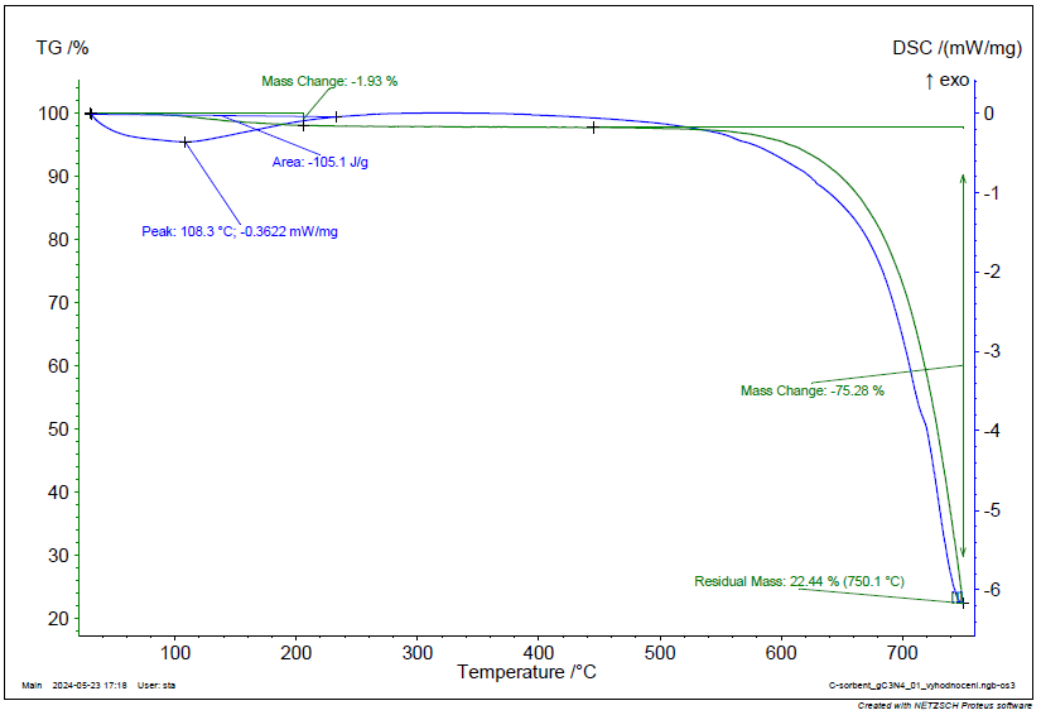

Figure 19. TGA and DSC analysis of g-C_3N_4.

3.2. Reaction with Polyethylene – Composite (g-C_3N_4, g-C_3N_4- PDA)

3.2.1. FT-IR Analysis

FTIR spectra of composites are presented on Figures 20-24.

 doi:10.20944/preprints202502.0474.v1

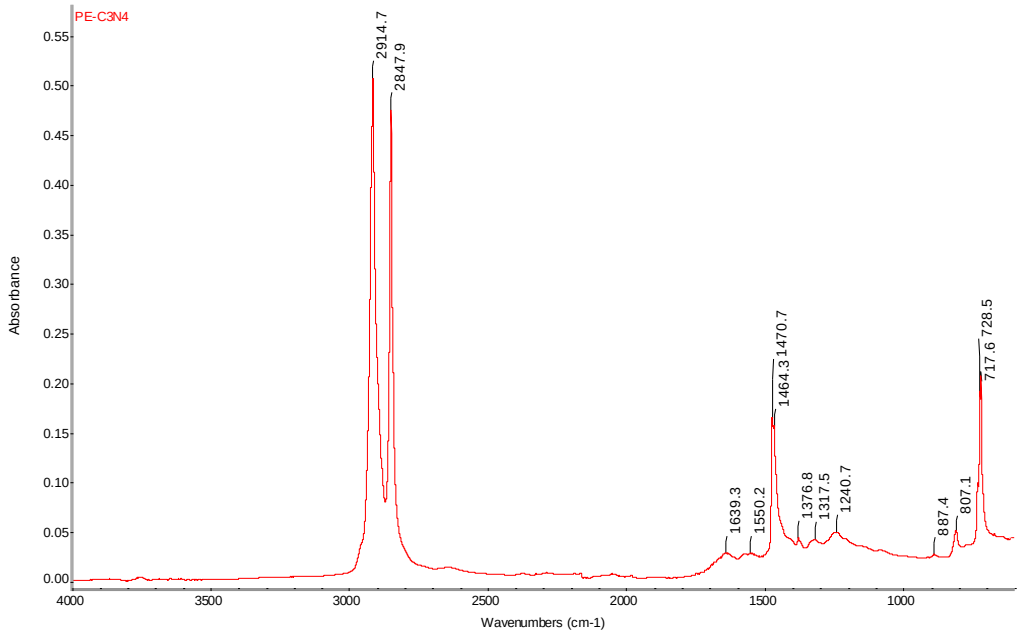

Figure 20. FTIR spectrum of PE-C_3N_4 with determination of characteristic bands.

Description – Figure 20:
Characteristic bands for PE:

2915 cm^{-1}	vibration $\nu_{as}(CH_2)$, bond $–CH_2$
2848 cm^{-1}	vibration $\nu_{s}(CH_2)$, bond $–CH_2$
1471 cm^{-1}	vibration $\delta(CH_2)$, bond $–CH_2$
718 cm^{-1} or 729 cm^{-1}	vibration $\varrho(CH_2)$, bond $–(CH_2)_n–$

Additional vibrations of PE: 1464 cm^{-1}, 1377 cm^{-1}, 887 cm^{-1}, 718 cm^{-1} or 729 cm^{-1}
Other bands:

1639 cm^{-1}, 1550 cm^{-1}	vibration C=N
1377 cm^{-1}, 1318 cm^{-1}, 1241 cm^{-1}	vibration C–N
807 cm^{-1}	vibration of CN cycle

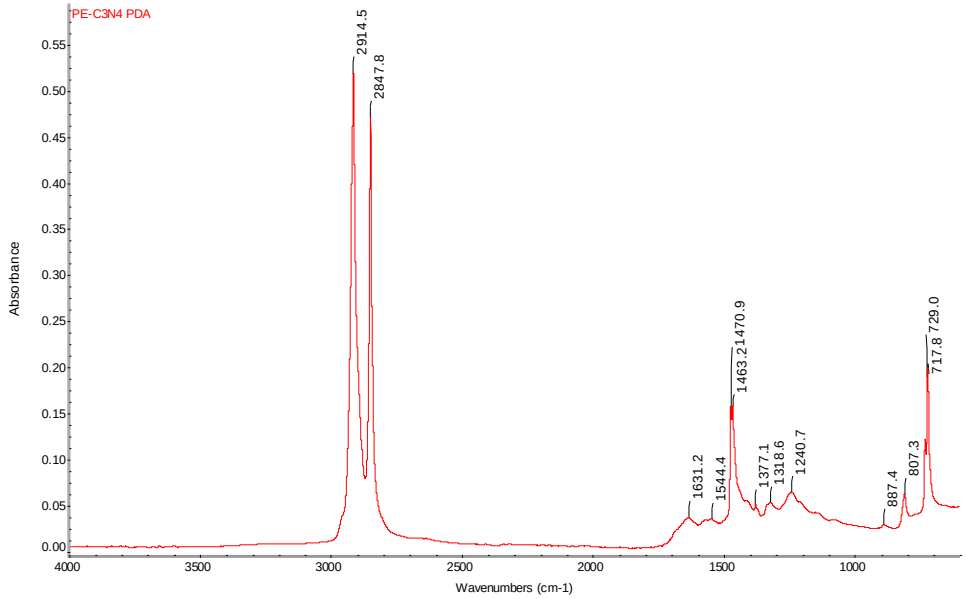

Figure 21. FTIR spectrum of PE-C_3N_4 PDA film with determination of characteristic bands.

a) Description – Figure 21:
Characteristic bands for PE:

 doi:10.20944/preprints202502.0474.v1

2915 cm^{-1} vibration $\nu_{as}(CH_2)$, bond $-CH_2$
2848 cm^{-1} vibration $\nu_{s}(CH_2)$, bond $-CH_2$
1471 cm^{-1} vibration $\delta(CH_2)$, bond $-CH_2$
718 cm^{-1} or 729 cm^{-1} vibration $\varrho(CH_2)_n-$
Additional vibrations of PE: 1463 cm^{-1}, 1377 cm^{-1}, 887 cm^{-1}, 718 cm^{-1} or 729 cm^{-1}
Other bands:
1631 cm^{-1}, 1544 cm^{-1} vibration C=N
1377 cm^{-1}, 1319; cm^{-1}, 1241 cm^{-1} vibration C–N
807 cm^{-1} vibration of CN cycle

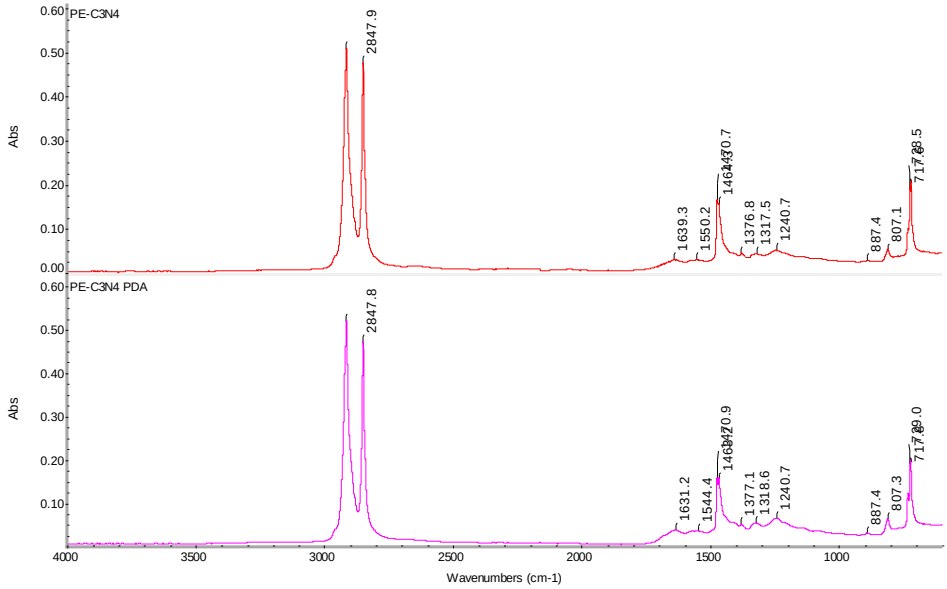

Figure 22. FTIR spectrum of PE-C_3N_4 and PE-C_3N_4 PDA films with determination of characteristic bands.

The next figure shows the FTIR spectrum of PP-gC_3N_4 filament with the determined band character and the comparison of g-C_3N_4 spectra.

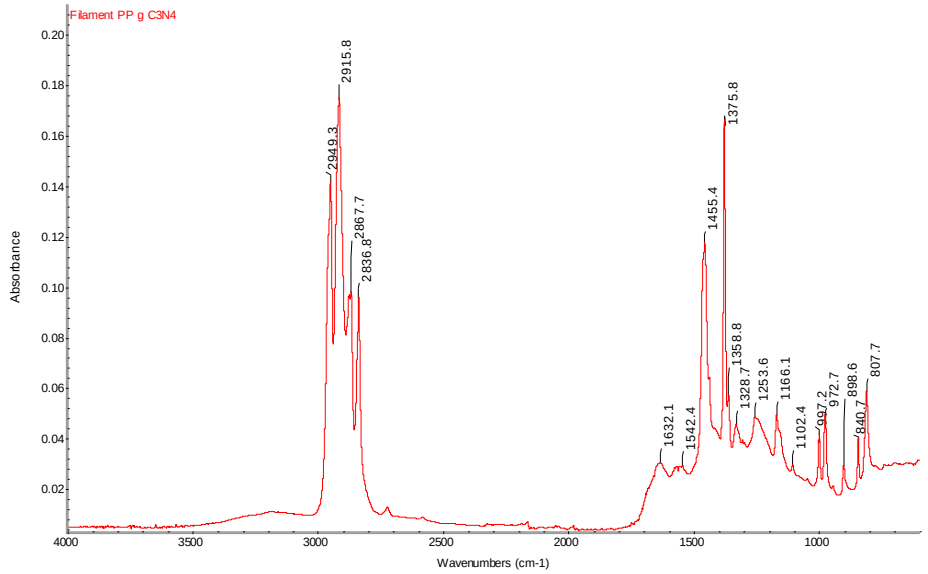

Figure 23. Infrared spectrum of PP g C_3N_4 filament sample with determination of characteristic bands.

a) Description – Figure 23:

Characteristic bands for PP:
2949 cm^{-1} vibration $\nu_{as}(CH_3)$, bond $-CH_3$

 doi:10.20944/preprints202502.0474.v1

2916 cm^{-1} vibration $\nu_{as}(CH_2)$, bond $-CH_2$
2876 cm^{-1} vibration $\nu_{s}(CH_3)$, bond $-CH_3$ (not marked in the spectrum)
2868 cm^{-1} vibration $\nu_{s}(CH_2)$, bond >CH–
2837 cm^{-1} vibration $\nu_{s}(CH)$, bond $-CH_2$
1455 cm^{-1} vibration $\delta_{as}(CH_3)$, bond $-CH_3$ or vibration $\delta(CH_2)$, bond $-CH_2$
1376 cm^{-1} vibration $\delta_{s}(CH_3)$, bond $-CH_3$
1166 cm^{-1} vibration $\delta(CH)$, bond $-CH$
997 cm^{-1} vibration $\delta(CH_3)$, bond $-CH_3$
973 cm^{-1} vibration δ for CH_3, CH_2 and CH
841 cm^{-1} vibration δ for CH_2 and $C-CH_3$
808 cm^{-1} chain vibration
1632 cm^{-1}, 1542 cm^{-1} not determined, this might be the vibration of the g-C_3N_4 component
Additional vibrations of PP: 1329 cm^{-1} (δCCH), 1254 cm^{-1} (δCH_2), 1102 cm^{-1}, 899 cm^{-1}(vibration C–C)

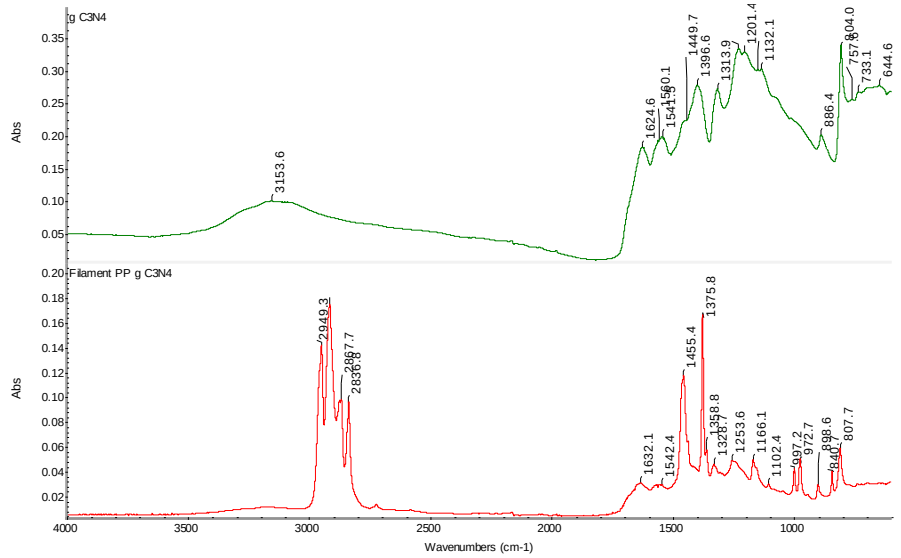

Figure 24. Comparison of FTIR spectra of initial gC_3N_4 and PP gC_3N_4 filament samples with determination of characteristic bands.

3.3.2. SEM Analysis

The microstructure of LDPE+g-C_3N_4 film is presented in Figure 25. The film appears to be smooth with the visible lighter aggregates of different size and shape, Figure 25 A. The estimated size/length of lighter spots is up to 10 μm. The higher magnification Figure 25 B and 25 C shows that the closest neighbourhood of spots is semi-disturbed. The film surface seems to be wrinkled similar to subtle waves (for the possible explanation see the notes below). The map of the elements distribution on the film surface is presented in Figure 26. Based on the registered maps it could be seen that the lighter spots are enriched in Nitrogen. The lack of Carbon at the same place is probably connected to the surface point-coverage by N. The microscopic images were taken with use of combined SE and BSE signals (SE+BSE). The heavier elements in BSE mode are represent in lighter shades of grey in comparison to less massive elements. In our research the Nitrogen (M = 14 g mol^{-1}) is slightly heavier than Carbon (M = 12 g mol^{-1}). Thus, based on the EDS maps and the SEM imaging techniques the lighter spots are quite certain connected to g-C_3N_4 particles.

 doi:10.20944/preprints202502.0474.v1

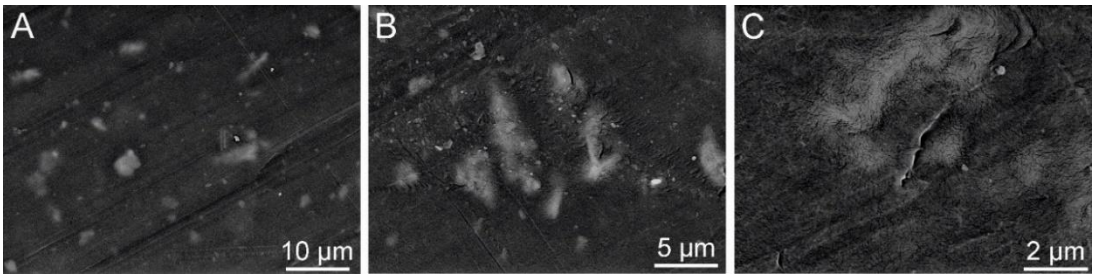

Figure 25. LDPE+g-C_3N_4 : SEM: SE+BSE A – the size of a scale bar 10 µm; B – 5 µm;C – 2 µm (Tesca Vegan 4).

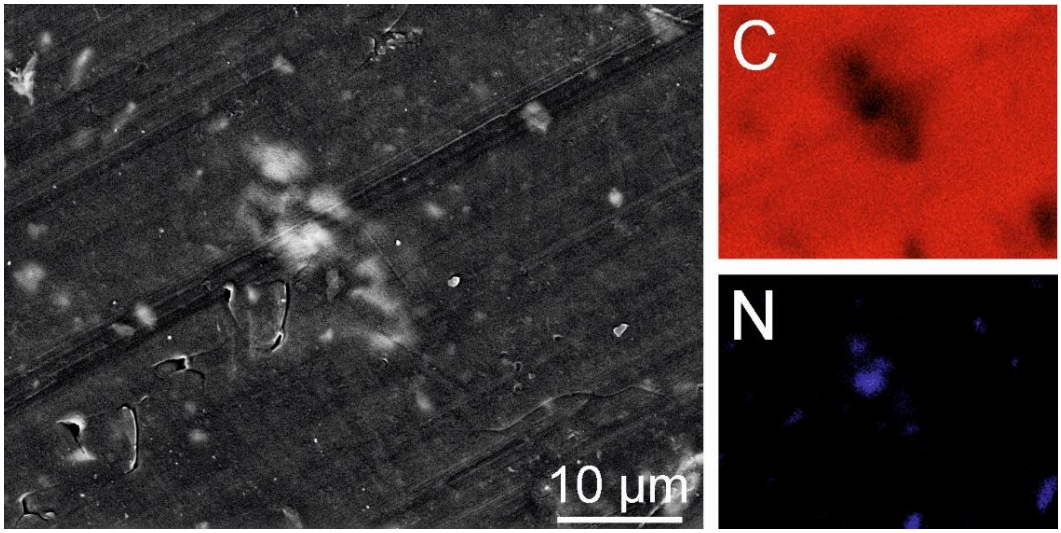

Figure 26. LDPE+C_3N_4 – EDS Mapping of C and N (Tesca Vegan 4).

3.2.3. TGA and DSC Analysis

For the polyethylene-10% g-C_3N_4 composite, TGA and DSC analysis revealed its decomposition from 190 °C to 490 °C in the form of three interconnected exothermic effects with the maximums at 262°C, 352°C and the main one at 407 °C (Figure 27). At the end of the tested temperature range, the exothermic effect at 696 °C can still be identified – the decomposition of C_3N_4.

For the polyethylene 10% g-C_3N_4-PDA composite, the main exothermic effect with the maximum at 420 °C (Figure 28) was preceded by the associated exothermic effect with the maximum at 267 °C, and the resulting weight loss for this exothermic effect is minimal at about 0.5%. The decomposition of this polymer composite occurs in the temperature range of 240-490 °C, which is a slight shift by about 50 °C compared to non-doped g-C_3N_4. Here again the exothermic effect is at 688 °C – the decomposition of g-C_3N_4.

 doi:10.20944/preprints202502.0474.v1

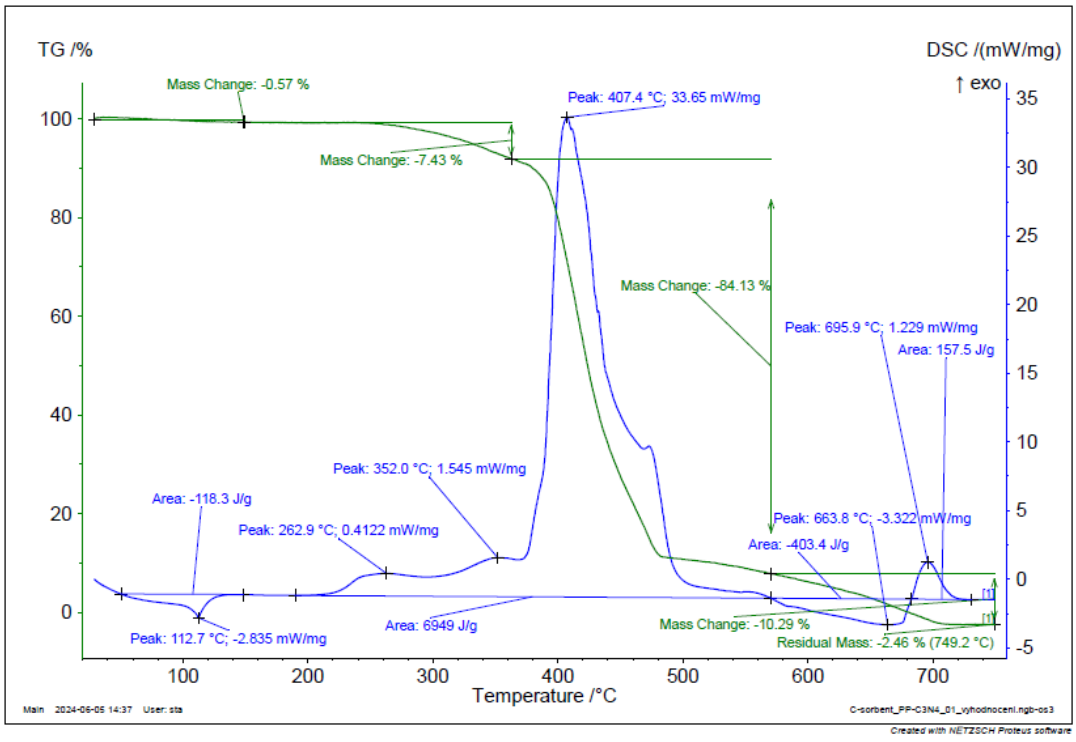

Figure 27. TGA and DSC analysis of g-C_3N_4-PE composite.

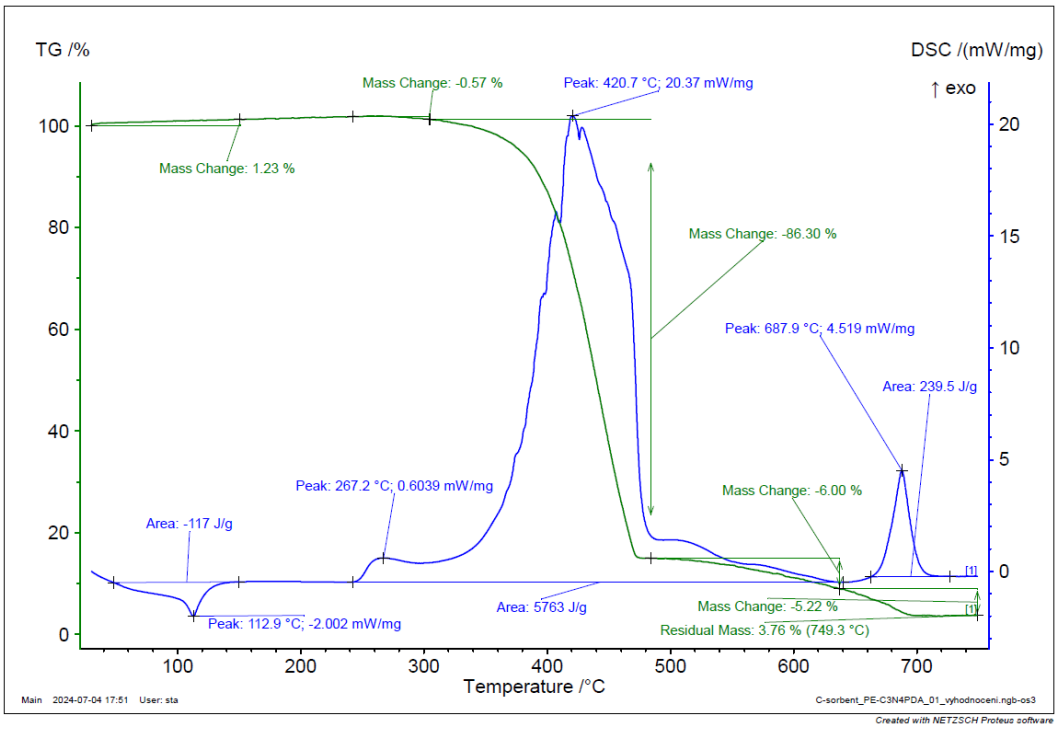

Figure 28. TGA and DSC analysis of g-C_3N_4-PDA-PE composite.

The thermal decomposition of the filament detected by TGA and DSC analysis, see Figure 29, associated with the weight loss of 90%, starts from the temperature of 240 °C with the exothermic effect with the maximum at 369 °C, and then the curve passes continuously through positive values into negative values, returns to positive values after about 300 °C, identifying the exothermic effect with the maximum at 698 °C in these values – the decomposition of C_3N_4.

 doi:10.20944/preprints202502.0474.v1

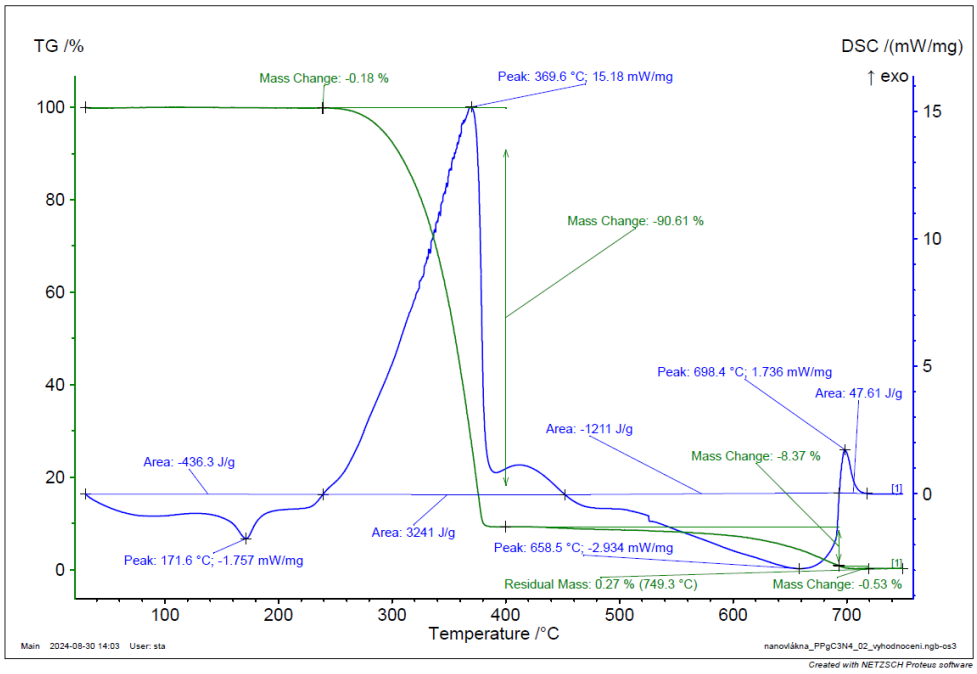

Figure 29. TGA and DSC analysis of PP-gC_3N_4 filament**.**

3.3. Nanofibers Prepared by DC and AC Electrospinning

SEM pictures of nanofibers prepared by DC and AX electrospinning are presented in Figures 30-33.

a) DC electrospinning - Nanospider™ (Elmarco, CZ)

3.3.1. SEM Analysis

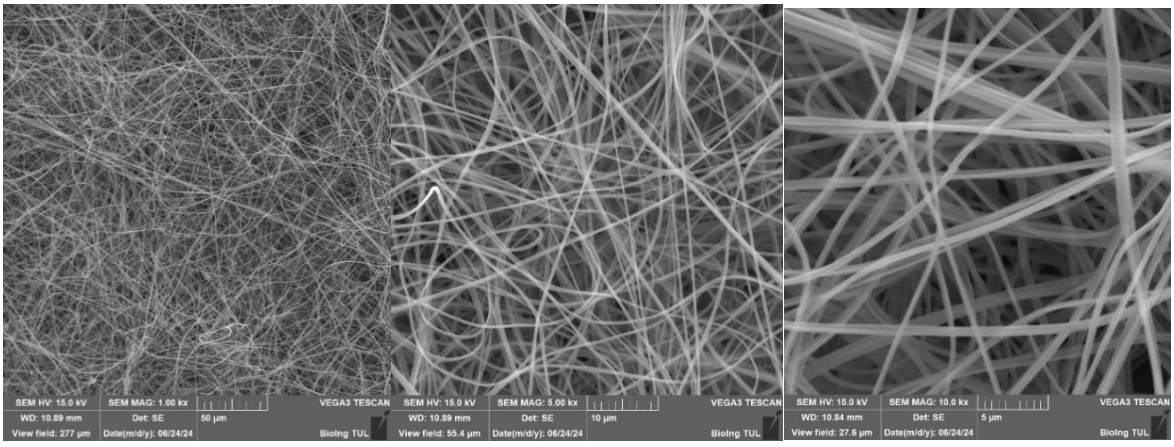

Figure 30. SEM analysis of PVB EL-DC nanofibers A – the size of a scale bar 50 *µm; B* – 10 *µm; C* - 5 *µm* (Tescan Vega 3 (TUL)).

 doi:10.20944/preprints202502.0474.v1

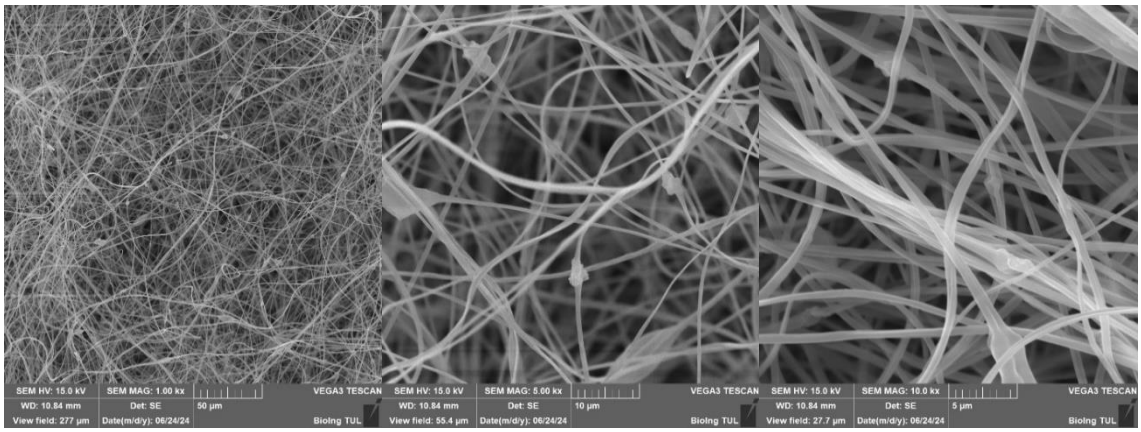

Figure 31. SEM analysis of PVB nanofiber with g-C_3N_4 EL-DC (A – the size of a scale bar 500 µm; B – 50 µm; C –5 µm) (Tesca Vegan 3 (TUL)).

b) AC electrospinning – rod electrode (TUL)

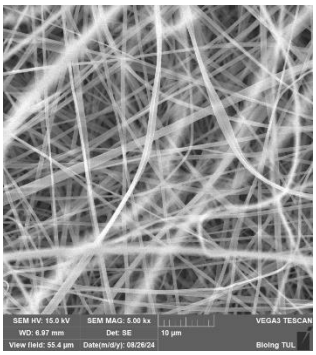

Figure 32. SEM analysis of PVB-EL-AC nanofibre (Tesca Vegan 3 (TUL)).

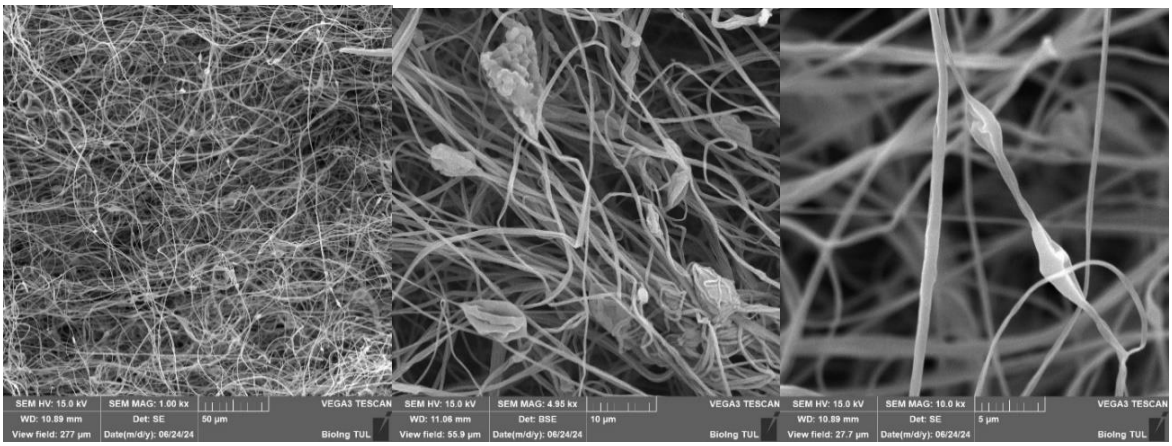

Figure 33. SEM analysis of PVB nanofibers with g-C_3N_4 EL-AC; A – magnification 50 µm; B – magnification 10 µm; C – magnification 5 µm (Tesca Vegan 3 (TUL)).

3.3.2. FT-IR Analysis

The nanofiber samples were subjected to FTIR, TGA and DSC analysis and the differences were also compared in relation to the spinning methodology (see FTIR samples in Figures 34-38).

 doi:10.20944/preprints202502.0474.v1

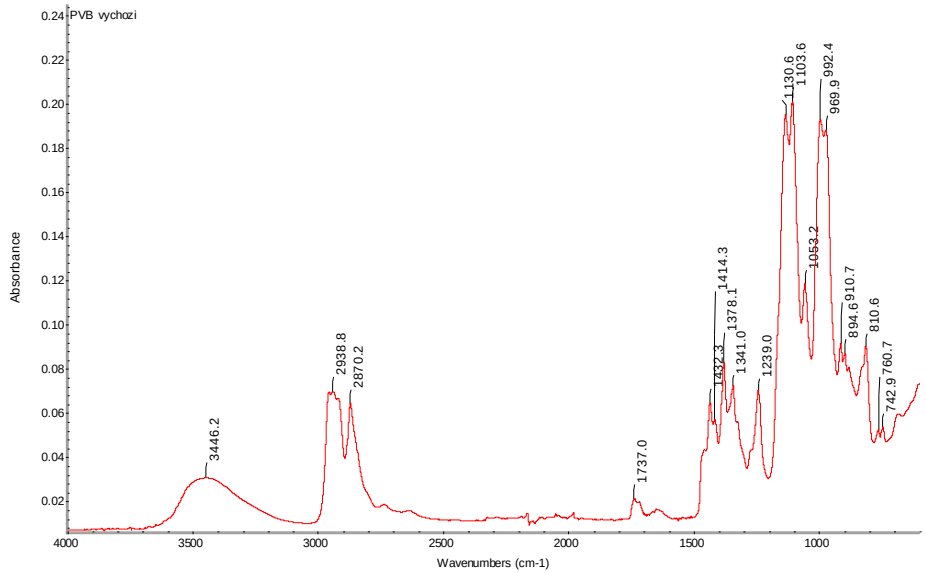

Figure 34. FTIR spectrum of initial PVB powder with determination of characteristic bands.

Description – Figure 34:

Characteristic bands for PVB:

3446 cm^{-1} vibration ν(OH), bond –OH

2955 cm^{-1} vibration νas(CH3), bond –CH3 (not marked in the spectrum)

Between the vibrations of 2955 cm^{-1} and 2870 cm^{-1}, visible "peaks" of the vibrations of $–CH_2$ and –CH bonds, e.g. 2939 cm^{-1}

2870 cm^{-1} vibration νs(CH3), bond –CH3

1737 cm^{-1} vibration ν(C=O), aldehydes

1432 cm^{-1}, 1414 cm^{-1}, 1378 cm^{-1}, 1341 cm^{-1}, 1239 cm^{-1}

vibration δ(CH2), bond –CH2 or vibration δ(CH3), bond –CH3 or vibration δ(COH)

1131 cm^{-1}, 1104 cm^{-1} vibration ν(COC)

1053 cm^{-1} vibration ν(CCO), primary alcohol

Additional vibrations of PVB: 992 cm^{-1}, 970 cm^{-1}, 911 cm^{-1}, 895 cm^{-1}, 878 cm^{-1} (not marked in the spectrum), 811 cm^{-1}, 761 cm^{-1}, 743 cm^{-1}

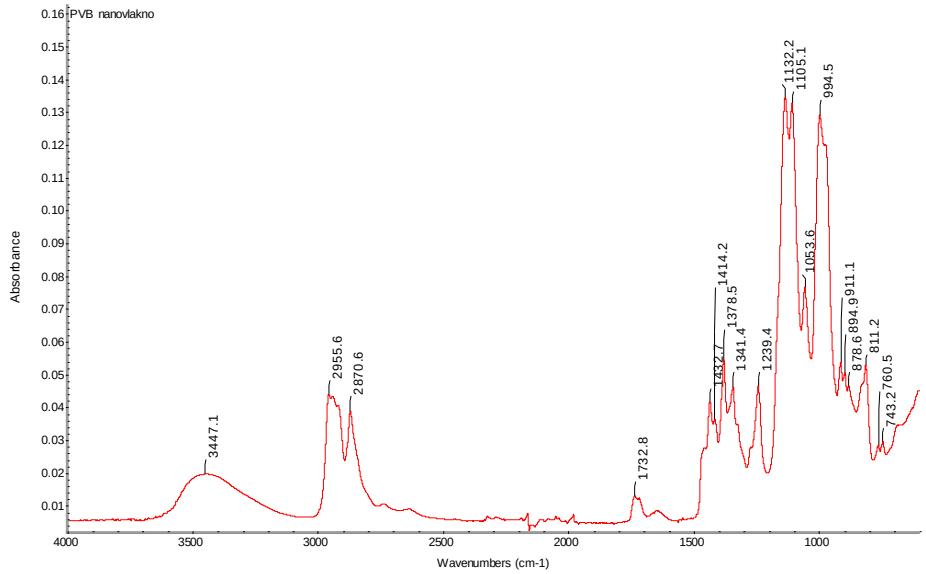

Figure 35. FTIR spectrum of pure PVB nanofibers with determination of characteristic AC electrospinning bands (AC-EL).

 doi:10.20944/preprints202502.0474.v1

c) Description – Figure 35:

Characteristic bands for PVB:

3447 cm^{-1} vibration ν(OH), bond –OH

2956 cm^{-1} vibration $\nu_{as}(CH_3)$, bond $–CH_3$

Between the vibrations of 2956 cm^{-1} and 2871 cm^{-1}, visible "peaks" of the vibrations of $–CH_2$ and –CH bonds

2871 cm^{-1} vibration $\nu_s(CH_3)$, bond $–CH_3$

1733 cm^{-1} vibration ν(C=O), aldehydes

1433 cm^{-1}, 1414 cm^{-1}, 1379 cm^{-1}, 1341 cm^{-1}, 1239 cm^{-1}

vibration $\delta(CH_2)$, bond $–CH_2$ or vibration $\delta(CH_3)$, bond $–CH_3$ or vibration δ(COH)

1132 cm^{-1}, 1105 cm^{-1} vibration ν(COC)

1054 cm^{-1} vibration ν(CCO), primary alcohol

Additional vibrations of PVB: 995 cm^{-1}, 972 cm^{-1} (not marked in the spectrum), 911 cm^{-1}, 895 cm^{-1}, 879 cm^{-1}, 811 cm^{-1}, 761 cm^{-1}, 743 cm^{-1}

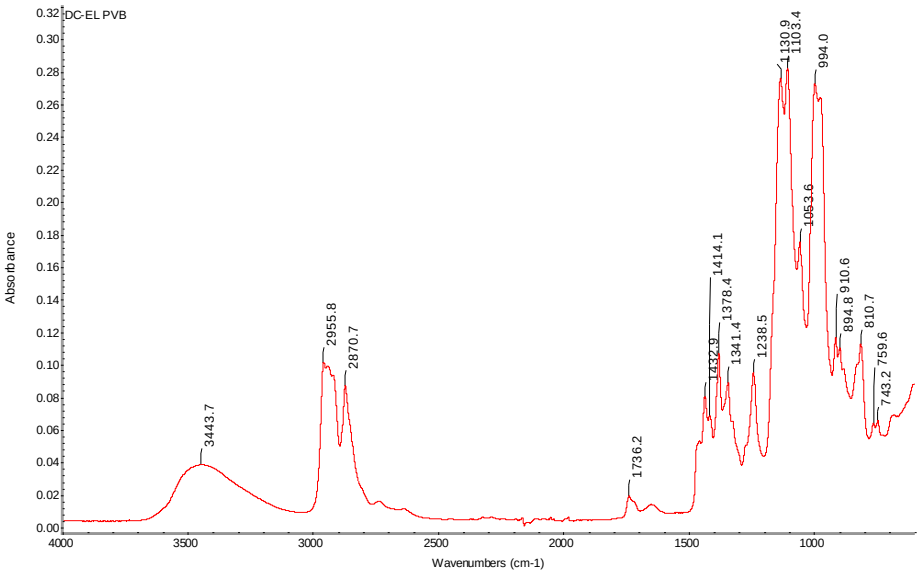

Figure 36. FTIR spectrum of pure PVB nanofibers with determination of characteristic DC electrospinning bands (DC-EL).

d) Description – Figure 36:

Characteristic bands for PVB:

3444 cm^{-1} vibration ν(OH), bond –OH

2956 cm^{-1} vibration $\nu_{as}(CH_3)$, bond $–CH_3$

Between the vibrations of 2956 cm^{-1} and 2871 cm^{-1}, visible "peaks" of the vibrations of $–CH_2$ and –CH bonds:

2871 cm^{-1} vibration $\nu_s(CH_3)$, bond $–CH_3$

1736 cm^{-1} vibration ν(C=O), aldehydes

1433 cm^{-1}, 1414 cm^{-1}, 1378 cm^{-1}, 1341 cm^{-1}, 1239 cm^{-1}

vibration $\delta(CH_2)$, bond $–CH_2$ or vibration $\delta(CH_3)$, bond $–CH_3$ or vibration δ(COH)

1131 cm^{-1}, 1103 cm^{-1} vibration ν(COC)

1054 cm^{-1} vibration ν(CCO), primary alcohol

Additional vibrations of PVB: 994 cm^{-1}, 911 cm^{-1}, 895 cm^{-1}, 811 cm^{-1}, 760 cm^{-1}, 743 cm^{-1}

 doi:10.20944/preprints202502.0474.v1

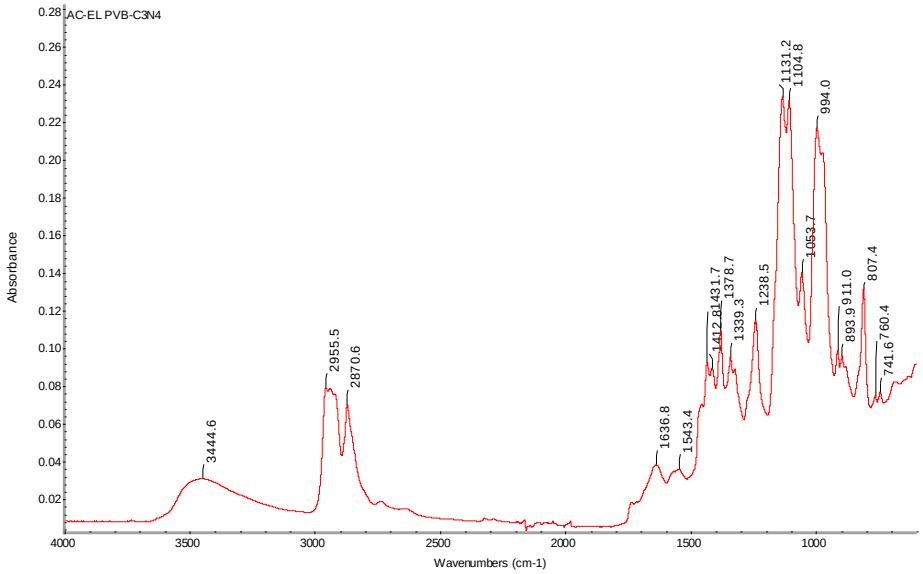

Figure 37. FTIR spectrum of nanofiber sample with PVB-C_3N_4 AC electrospinning (AC-EL) with determination of characteristic bands**.**

e) Description – Figure 37:

Characteristic bands for PVB:

3445 cm^{-1} vibration ν(OH), bond –OH

2956 cm^{-1} vibration $\nu_{as}(CH_3)$, bond $–CH_3$

Between the vibrations of 2956 cm^{-1} and 2871 cm^{-1}, visible "peaks" of the vibrations of $–CH_2$ and –CH bonds

2871 cm^{-1} vibration $\nu_s(CH_3)$, bond $–CH_3$

1432 cm^{-1}, 1413 cm^{-1}, 1379 cm^{-1}, 1339 cm^{-1}, 1239 cm^{-1}

vibration $\delta(CH_2)$, bond $–CH_2$ or vibration $\delta(CH_3)$, bond $–CH_3$ or vibration δ(COH)

1131 cm^{-1}, 1105 cm^{-1} vibration ν(COC)

1054 cm^{-1} vibration ν(CCO), primary alcohol

Negligible band 1735 cm^{-1} for vibrations ν(C=O), aldehydes

Additional vibrations of PVB: 994 cm^{-1}, 911 cm^{-1}, 894 cm^{-1}, 807 cm^{-1}, 760 cm^{-1}, 742 cm^{-1}

Other bands:

1637 cm^{-1}, 1543 cm^{-1} vibration C=N

1432 cm^{-1}, 1413 cm^{-1}, 1379 cm^{-1}, 1339 cm^{-1}, 1239 cm^{-1}

The above vibrations or C-N vibrations

807 cm^{-1} band for PVB or vibrations of the CN cycle

 doi:10.20944/preprints202502.0474.v1

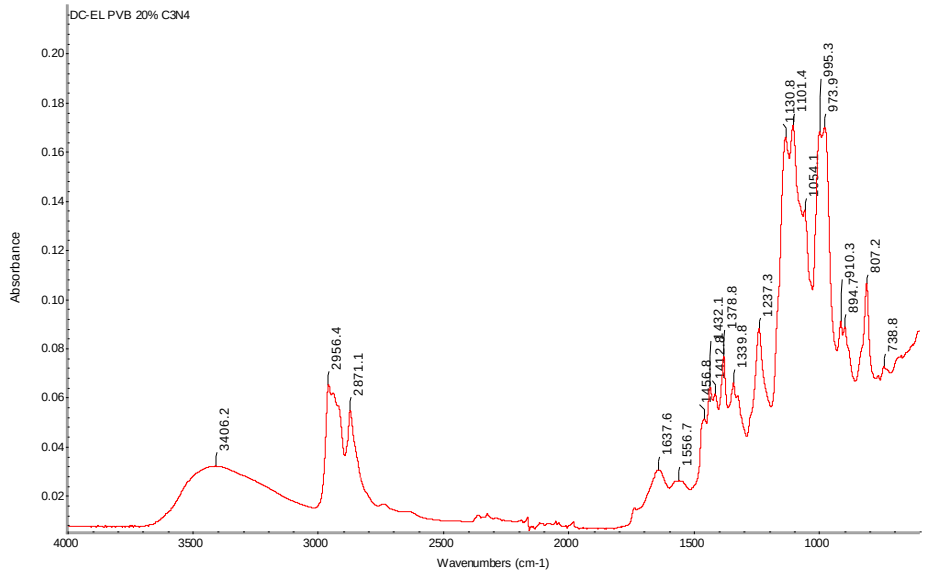

Figure 38. FTIR spectrum of PVB 20% C_3N_4 DC-EL nanofiber sample with determination of characteristic bands.

f) Description – Figure 38:

Characteristic bands for PVB:

3406 cm^{-1} vibration ν(OH), bond –OH

2956 cm^{-1} vibration $\nu_{as}(CH_3)$, bond $–CH_3$

Between the vibrations of 2956 cm^{-1} and 2871 cm^{-1}, visible "peaks" of the vibrations of $–CH_2$ and –CH bonds

2871 cm^{-1} vibration $\nu_s(CH_3)$, bond $–CH_3$

1432 cm^{-1}, 1413 cm^{-1}, 1379 cm^{-1}, 1340 cm^{-1}, 1237 cm^{-1}

vibration $\delta(CH_2)$, bond $–CH_2$ or vibration $\delta(CH_3)$, bond $–CH_3$ or vibration δ(COH)

1131 cm^{-1}, 1101 cm^{-1} vibration ν(COC)

1054 cm^{-1} vibration ν(CCO), primary alcohol

Additional vibrations of PVB: 995 cm^{-1}, 974 cm^{-1}, 910 cm^{-1}, 895 cm^{-1}, 807 cm^{-1}, 739 cm^{-1}

Other bands:

1638 cm^{-1}, 1557 cm^{-1} vibration C=N

1432 cm^{-1}, 1413 cm^{-1}, 1379 cm^{-1}, 1340 cm^{-1}, 1237 cm^{-1} the above vibrations or C-N vibrations

807 cm^{-1} band for PVB or vibrations of the CN cycle

The measured FTIR spectra were from the initial graphitic carbon nitride g-C_3N_4, from g-C_3N_4-free polyvinyl butyral nanofibers fabricated by DC electrospinning. Further nanofiber spectra were already taken with the g-C_3N_4 composite, but using a different spinning technique.

3.3.3. TGA and DSC Analysis

The graphic carbon nitride decomposes with endothermic effect with the maximum at 748 °C, the beginning of the endothermic effect is at 565 °C, which immediately passes to the exothermic effect at 772°C (Figure 39).The nanofiber spun from polyvinyl butyral (PVB) by DC electrospinning decomposes over a wide temperature range from 225 °C to 600 °C with a continuous exothermic effect identified with six maximums at 331 °C, 386 °C, 414 °C, 495 °C, 520 °C and 534 °C in the energy range of 2-6 mW/mg (Figure 4**0**). This composite, prepared by DC spinning, decomposes in the temperature range from 275 °C to 550 °C with the weight loss of 76% with a low heat flow compared to pure PVB – for comparison see Figure **40** and Figure **42** . In contrast, the exothermic effect was identified with a strong energy flow (17 mW mg^{-1}) with the maximum at 616 °C and the weight loss of 14% (Figure **41**). A different spectrum from thermographic analysis was obtained from the PVB-g-C_3N_4 composite obtained by AC spinning (Figure 43). Two exothermic effects with maximums at 402

 doi:10.20944/preprints202502.0474.v1

°C and 495 °C are separately identified in the spectrum, which pass to the endothermic effect with the maximum at 625 °C followed by the exothermic effect at 693 °C.

The interaction between the composite and the polymer resulted, for example, in the decrease in maximum values for both the endothermic effect and the exothermic effect. The effect of the spinning method on the behaviour of composite nanofibre during thermal stress has been also shown. We assume suppression of, for example, g-C_3N_4 sublimation

TGA and DSC of PVB powder is presented in Figure 44. For clarity, the affected spectra of the TGA and DSC analysis are shown in the following pyramid scheme (see Figures A1 and Figures A2 in Supplementary).

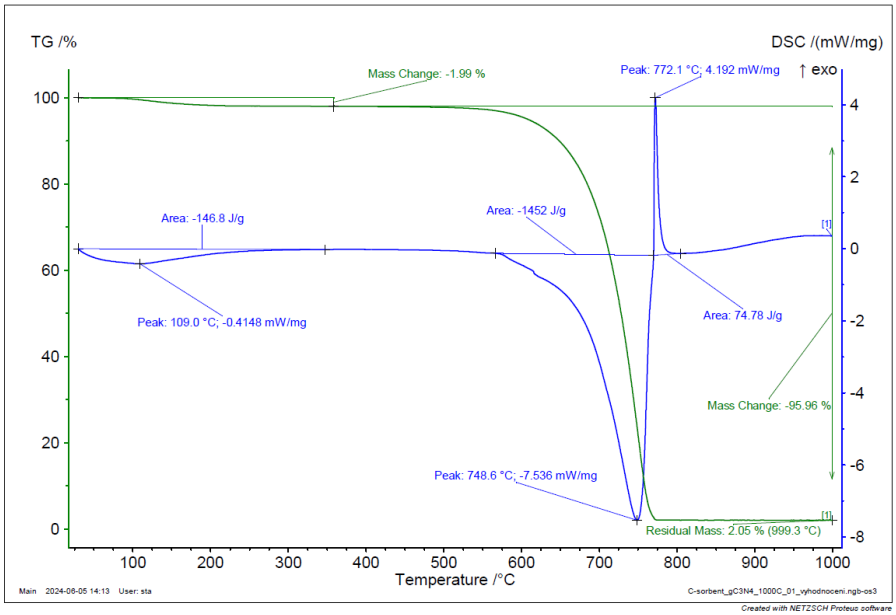

Figure 39. TGA and DSC analysis of g-C_3N_4 sample**.**

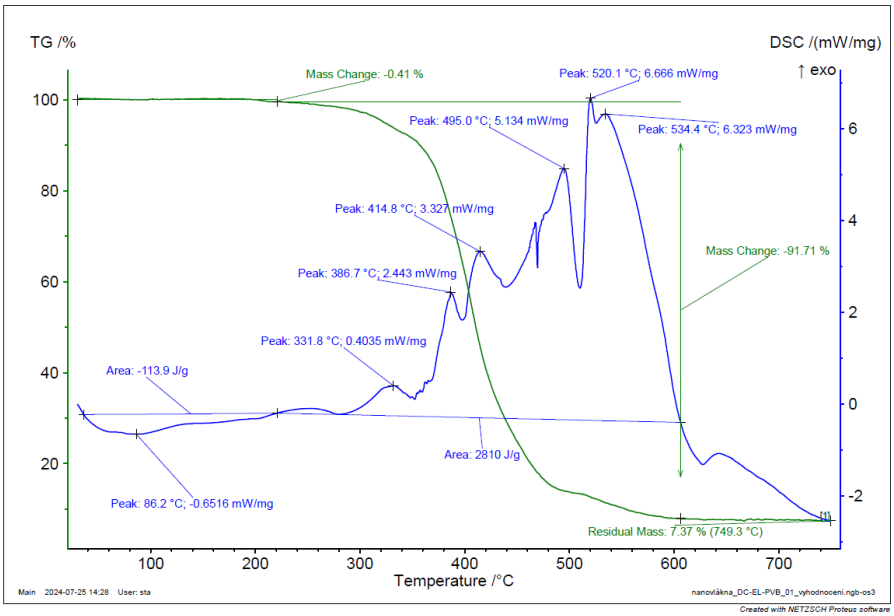

Figure 40. TGA and DSC analysis of PVB EL-DC nanofiber**.**

 doi:10.20944/preprints202502.0474.v1

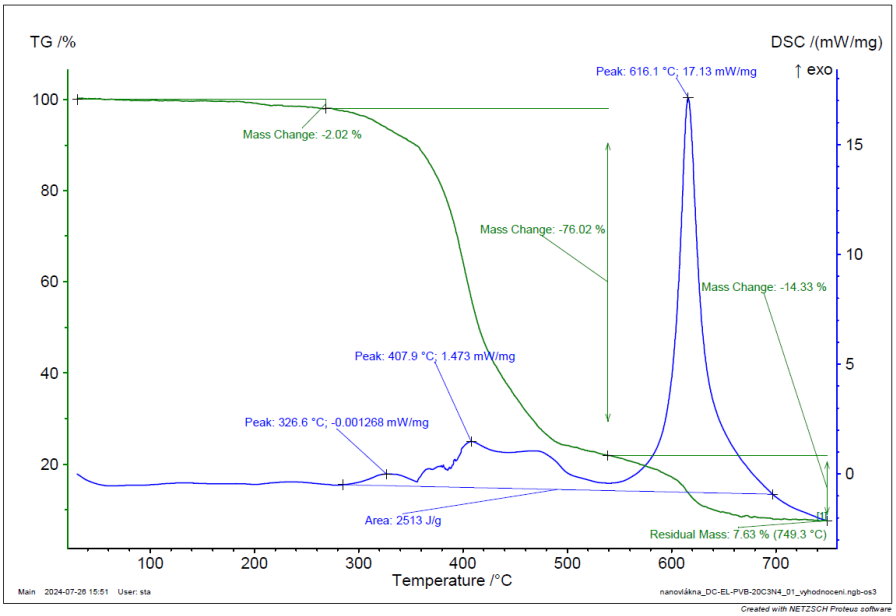

Figure 41. TGA and DSC analysis of PVB-C_3N_4 EL-DC nanofiber.

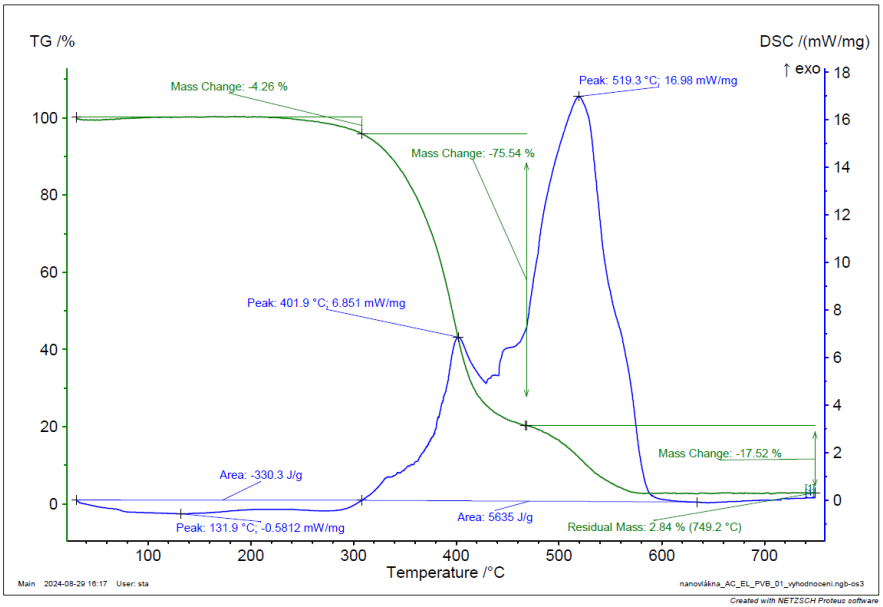

Figure 42. TGA and DSC analysis of PVB EL-AC nanofiber.

 doi:10.20944/preprints202502.0474.v1

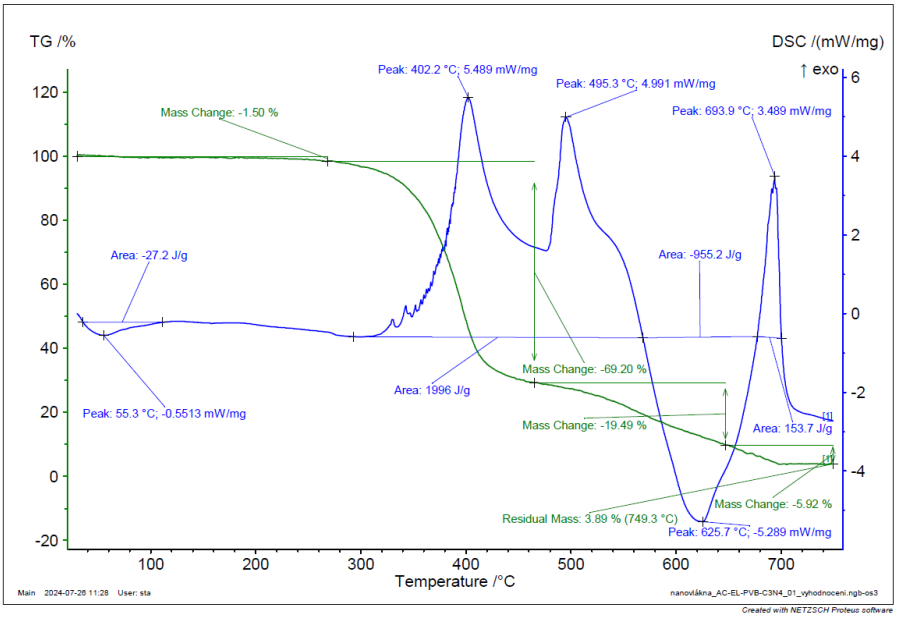

Figure 43. TGA and DSC analysis of PVB-C_3N_4-EL-AC nanofiber.

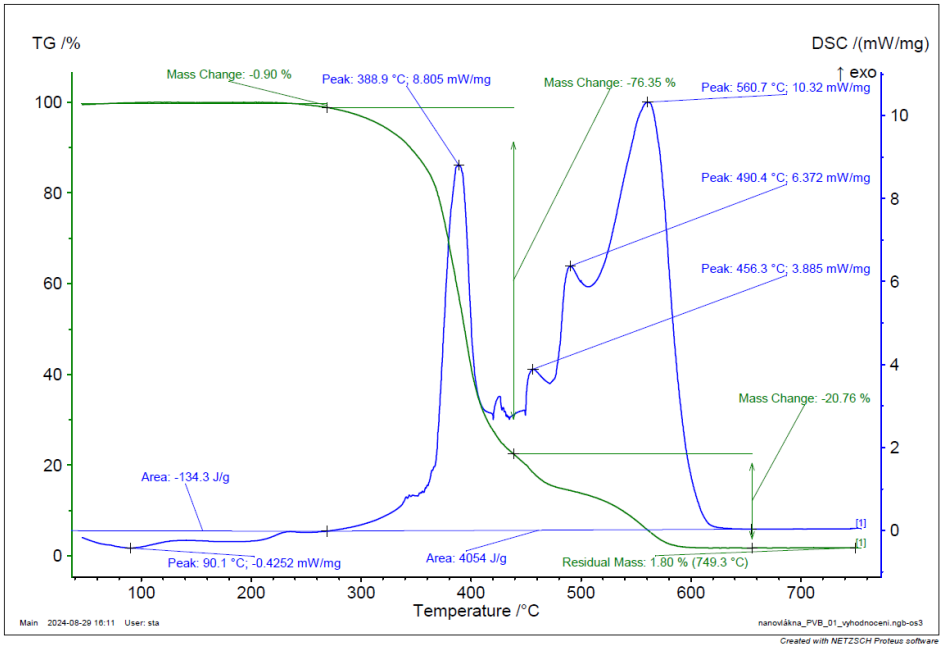

Figure 44. TGA and DSC of PVB powder.

4. Conclusions

The aim of this work was to investigate the thermal stability of g- C_3N_4 and its modifications. First, the preparation of g-C3N4 and further reactions with various modifications of GO (graphene oxide) and other materials are described. The following section focuses on the description of electrospinning using direct and alternating current with attention to the differences between these fabrication techniques. The first part of the experimental results of the work focuses on doped g- C_3N_4 (GO, Fe_2O_3, H_2O_2, etc.) presented by FT-IR analyses of the different materials and modifications, then SEM analyses using different magnifications are also presented, with clear differences in the structures of the different modifications. Finally, TGA analyses are described, the purpose of which was to test the response of the materials to thermal decomposition. The second part of the experiments is described in analogy to the first part, the only difference being the use and comparison

 doi:10.20944/preprints202502.0474.v1

of plastic composites (PP, PE, LDPE, PVB). FT-IR analyses, SEM and TGA/DSC analyses are presented. The main objective of this work was to modify the prepared g- C_3N_4 in such a way that the photocatalytic capabilities of this material and the prepared modifications can be tested in the planned follow-up experiments. The possible use in reactions under the simultaneous application of a magnetic field without light access will also be tested.

Author Contributions: For research articles with several authors, a short paragraph specifying their individual contributions must be provided. The following statements should be used "Conceptualization, K.K. and P.R.; methodology, K.K.; validation, K.G., R.F. and Z.Z.; formal analysis, K.B.; investigation, M.V.;P.B.;K.G.;E. K.K.; Z.S.; resources, J.T.; data curation, K.K.; writing—original draft preparation, K.K.; writing—review and editing, P.R.; visualization, K.K.; supervision, K.K.; All authors have read and agreed to the published version of the manuscript." Please turn to the CRediT taxonomy for the term explanation. Authorship must be limited to those who have contributed substantially to the work reported.

Funding: This research received no external funding.

Data Availability Statement: : "Not applicable".

Conflicts of Interest: The authors declare no conflicts of interest.

Appendix A

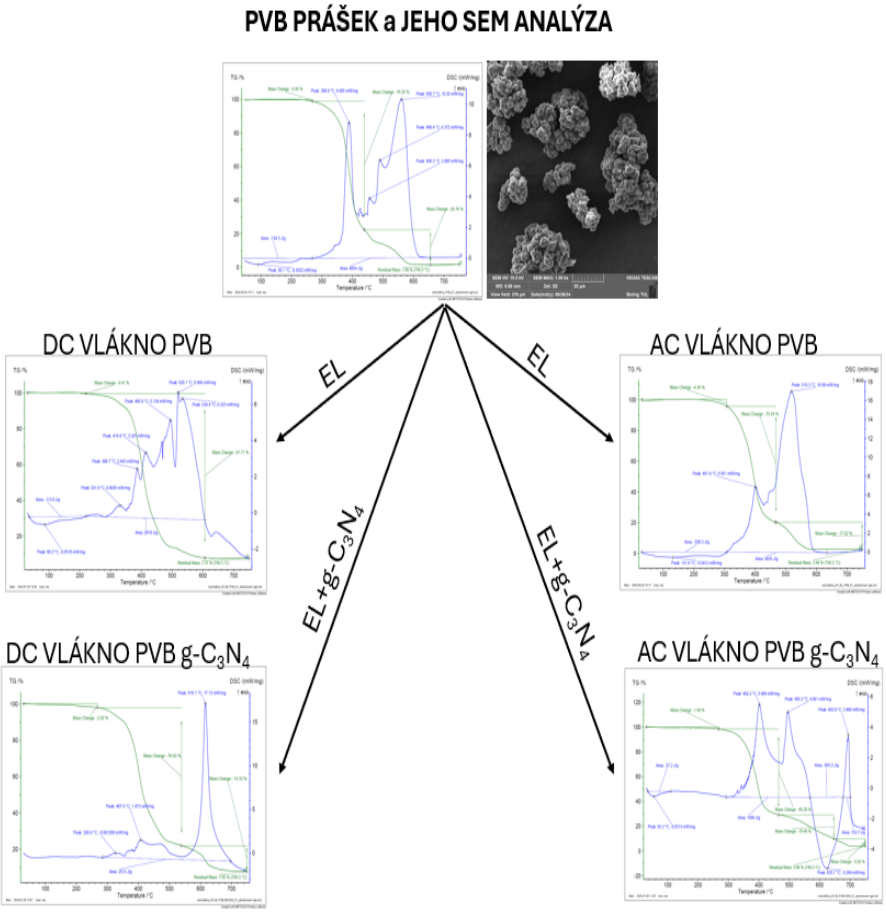

Figure A1. TGA and DSC analysis of initial PVB and prepared fibers without and with g-C_3N_4.

 doi:10.20944/preprints202502.0474.v1

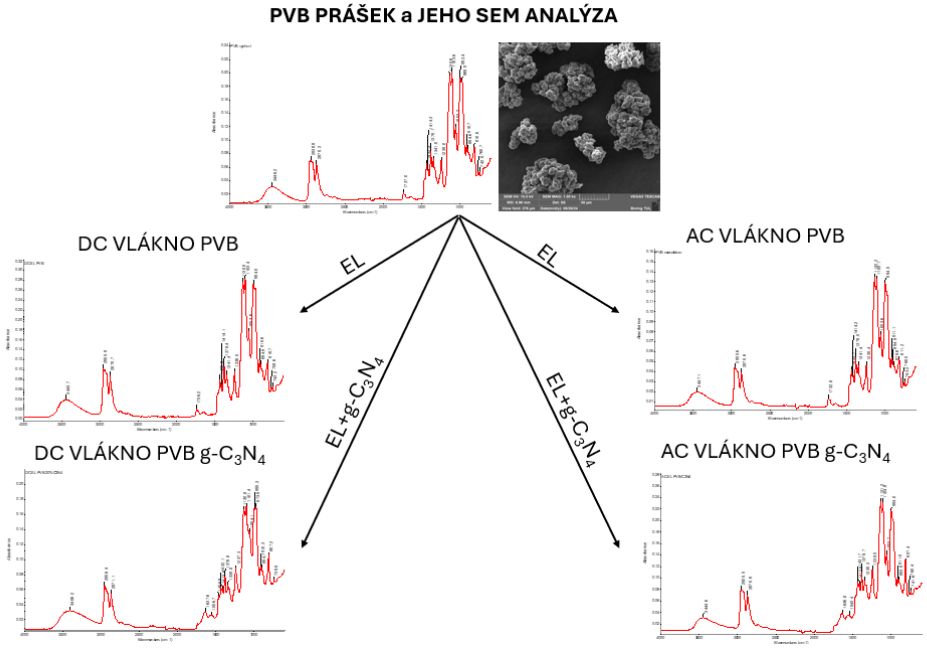

Figure A2. FTIR spectra of initial PVB and prepared fibers with and without g-C_3N_4.

Findings after spectrum comparison could be found in Tables 1 and 2.

Table 1. Temperature range required to achieve product distribution.

Product name	**Temperature [°C]**	**Residues [%]**
PVB – powder	380	1.8
PVB – DC fiber	390	7.3
PVB – AC fiber	326	2.8
For the 1st and 3rd samples, the difference is 54°C		
PVB DC fiber g-C_3N_4	412	7.6
PVB AC fiber g-C_3N_4	460	3.8

The lowest temperature range where product decomposition occurs was measured for AC nanofiber, the initial powder has the value comparable to DC nanofiber. Both composites have a greater temperature range, up to 80 °C, compared to the initial powder.

Table 2. Number of maximums for the product and thermal effect during decomposition.

Product name	**Number of maximums**	**Thermal effect** [mW mg^{-1}]
PVB – powder	4	29.382
PVB – DC fiber	6	24.296
PVB – AC fiber	2	23.831
PVB DC fiber g-C_3N_4	2	18.603
PVB AC fiber g-C_3N_4	3 + 1 *	8.680

* maximum during endothermic effect.

References

1. Singh, P.; Srivastava, V. Recent advances in visible-light graphitic carbon nitride (g-C3N4) photocatalysts for chemical transformations. *RSC Adv.* **2022**, *12*, 18245–18265. doi: 10.1039/D2RA01797K.
2. Qamar, M.A.; Javed, M.; Shahid, S.; Shariq, M.; Fadhali, M.M.; Ali, S.K.; Khan, M.S. Synthesis and applications of graphitic carbon nitride (g-C3N4) based membranes for wastewater treatment: A critical review. *Heliyon* **2023**, *9* (1), ISSN 2405-8440. doi:10.1016/j.heliyon.2022.e12685.

3. Chen, Y.; Lu, C. Graphitic carbon nitride nanomaterials for high-performance supercapacitors. *Carbon Neutralization* **2023**, *2*, 585–602. doi:10.1002/cnl2.87.
4. Miao, Z.; Wu, G.; Wang, Q.; Yang, J.; Wang, Z.; Yan, P.; Sun, P.; Lei, Y.; Mo, Z.; Xu, H. Recent advances in graphitic carbon nitride-based photocatalysts for solar-driven hydrogen production. *Mater. Rep. Energy* **2023**, *3* (4), 100235. ISSN 2666-9358. doi:10.1016/j.matre.2023.100235.
5. Li, Y.; Zhu, S.; Liang, Y.; Li, Z.; Wu, S.; Chang, C.; Cui, Z. Synthesis of α-Fe2O3/g-C3N4 photocatalyst for high-efficiency water splitting under full light. *Mater. Des.* **2020**, *109191*. doi:10.1016/j.matdes.2020.109191.
6. Chen, M.M.A.; Li, M.; Qiu, X. Synthesis and modification strategies of g-C3N4 nanosheets for photocatalytic applications. *Adv. Powder Mater.* **2024**, *3*, doi:10.1016/j.apmate.2023.100150.
7. Li, X.; Huang, G.; Chen, X.; Huang, J.; Li, M.; Yin, J.; Li, Y. A review on graphitic carbon nitride (g-C3N4) based hybrid membranes for water and wastewater treatment. *Sci. Total Environ.* **2021**, *792*, 148462. doi:10.1016/j.scitotenv.2021.148462-
8. Vasiljević, J.; Jerman, I.; Simončič, B. Graphitic carbon nitride as a new sustainable photocatalyst for textile functionalization. *Polymers* **2021**, *13* (15), 2568. https://doi.org/10.3390/polym13152568.
9. Zhang, M.; Yang, Y.; An, X.; Hou, L. A critical review of g-C3N4-based photocatalytic membrane for water purification. *Chem. Eng. J.* **2021**, *412*, 128663. doi:10.1016/j.cej.2021.128663.
10. Oluwole, A.; Khoza, P.; Olatunji, O.S. Synthesis and characterization of g-C3N4 doped with activated carbon (AC) prepared from grape leaf litters for the photocatalytic degradation of enrofloxacin in aqueous systems. *ChemistrySelect* **2022**, *7* (45), e202203601.
11. Huang, J.; Hu, J.; Shi, Y.; Zeng, G.; Cheng, W.; Yu, H.; Yi, K. Evaluation of self-cleaning and photocatalytic properties of modified g-C3N4 based PVDF membranes driven by visible light. *J. Colloid Interface Sci.* **2019**, doi:10.1016/j.jcis.2019.01.105.
12. Khurram, R.; Nisa, Z.; Javed, A.; Wang, Z.; Hussien, M. Synthesis and characterization of an Fe2O3-decorated g-C3N4 heterostructure for the photocatalytic removal of MO. *Molecules* **2022**, *27*, 1–18. doi:10.3390/molecules270414428.
13. Manickam, R.; Kokilavani, S.; Khan, S. Recent developments in architecturing the g-C3N4 based nanostructured photocatalysts: Synthesis, modifications and applications in water treatment. *Chemosphere* **2021**, *291*.
14. Rajeshwari, M.R.; Kokilavani, S.; Khan, S. Recent developments in architecturing the g-C3N4 based nanostructured photocatalysts: Synthesis, modifications and applications in water treatment. *Chemosphere* **2022**, *291* (Pt 1), 132735.
15. Zhang, S.; Gu, P.; Ma, R.; Luo, C.; Wen, T.; Zhao, G.; Wang, X. Recent developments in fabrication and structure regulation of visible-light-driven g-C3N4-based photocatalysts towards water purification: A critical review. *Catal. Today* **2018**, doi:10.1016/j.cattod.2018.09.013.
16. Ding, M.; Qu, Y.; Zhang, X.; Duan, L.; Li, X.; Lü, W. Reduced graphene oxide/g-C3N4 modified carbon fibers for high performance fiber supercapacitors. *New J. Chem.* **2021**, *45* (2), 923–929. doi:10.1039/d0nj05072e.
17. Dong, J.; Zhang, Y.; Hussain, M.I.; Zhou, W.; Chen, Y.; Wang, L.N. g-C3N4: Properties, pore modifications, and photocatalytic applications. *Nanomaterials* (Basel, Switzerland) **2021**, *12* (1), 121. https://doi.org/10.3390/nano12010121.
18. Bhanderi, D.; Lakhani, P.; Modi, C. Graphitic carbon nitride (g-C3N4) as an emerging photocatalyst for sustainable environmental applications: A comprehensive review. *RSC Sustainability* **2023**, *2*, 10.1039/d3su00382e.
19. Roupcová, P. Monitoring of the ecotoxicity of the carbon based nanoparticles. Dissertation Thesis, VSB – Technical University of Ostrava, Faculty of Safety Engineering, **2018**.
20. Bytešníková, Z.; Birgusová, E.; Pekárková, J.; Švec, P.; Richtera, L. A novel method for modification of poly(lactic acid) filament by graphene oxide for 3D print. In *Proceedings 15th International Conference on Nanomaterials - Research & Application*; **2023**; pp. 298–302. ISBN 978-80-88365-15-0. ISSN 2694-930X. doi: 10.37904/nanocon.2023.4799.

21. Vilamová, Z.; Sampaio, M.J.; Svoboda, L.; Bednář, J.; Simonova, Z.; Dvorsky, R.; Silva, C.G.; Faria, J.L. Enhancing Photocatalytic g-C3N4/PVDF membranes through new insights into the preparation methods. *Polymer* **2024**, *307*, 127238. https://doi.org/10.1016/j.polymer.2024.127238
22. Vilamová, Z.; Czernek, P.; Zágora, J.; Svoboda, L.; Bednář, J.; Simonova, Z.; Placha, D.; Dvorsky, R. Fibrous PVDF membranes modified by anchored g-C3N4@GO composite with enhanced photocatalytic activity. *Appl. Surf. Sci.* **2024**, *677*, 161055. doi:10.1016/j.apsusc.2024.161055.
23. Wang, H.; Xu, Y.; Wei, Q. Preparation of bamboo-hat-shaped deposition of a poly(ethylene terephthalate) fiber web by melt-electrospinning. *Text. Res. J.* **2015**, *85*, 1838–1848.
24. Reneker, D. H.; Yarin, A. L.; Zussman, E.; Xu, H. Electrospinning of nanofibers from polymer solutions and melts. *Adv. Appl. Mech.* **2007**, *41*, 43–346.
25. Li, D.; Xia, Y. Electrospinning of nanofibers: reinventing the wheel? *Adv. Mater.* **2004**, *16*, 1151–1170.
26. Lomov, S. V.; Molnár, K. Compressibility of carbon fabrics with needleless electrospun PAN nanofibrous interleaves. *Express Polym. Lett.* **2015**, *10*, 25–35.
27. Nagy, Z. K.; Balogh, A.; Démuth, B.; Pataki, H.; Vigh, T.; Szabó, B.; Molnár, K.; Schmidt, B. T.; Horák, P.; Marosi, G.; Verreck, G.; Van Assche, I.; Brewster, M. E. High speed electrospinning for scaled-up production of amorphous solid dispersion of itraconazole. *Int. J. Pharm.* **2015**, *480*, 137–142.
28. Balogh, A.; Horváthová, T.; Fülöp, Z.; Loftsson, T.; Harasztos, A. H.; Marosi, G.; Nagy, Z. K. Electroblowing and electrospinning of fibrous diclofenac sodium-cyclodextrin complex-based reconstitution injection. *J. Drug Deliv. Sci. Technol.* **2015**, *26*, 28–34.
29. Pokorny, P.; Kostakova, E.; Sanetrnik, F.; Mikes, P.; Chvojka, J.; Kalous, T.; Bilek, M.; Pejchar, K.; Valtera, J.; Lukas, D. Effective AC needleless and collectorless electrospinning for yarn production. *Phys. Chem. Chem. Phys.* **2014**, *16*, 26816–26822.
30. Lawson, C.; Stanishevsky, A.; Sivan, M.; Pokorny, P.; Lukáš, D. Rapid fabrication of poly(ε-caprolactone) nanofibers using needleless alternating current electrospinning. *J. Appl. Polym. Sci.* **2016**, *133*.
31. Balogh, A.; Farkas, B.; Verreck, G.; Mensch, J.; Borbás, E.; Nagy, B.; Marosi, G.; Nagy, Z. K. AC and DC electrospinning of hydroxypropylmethylcellulose with polyethylene oxides as secondary polymer for improved drug dissolution. *Int. J. Pharm.* **2016**, *505*, 159–166. doi:10.1016/j.ijpharm.2016.03.024.
32. Sun, B.; Long, Y. Z.; Zhang, H. D.; Li, M. M.; Duvail, J. L.; Jiang, X. Y.; Yin, H. L. Advances in three-dimensional nanofibrous macrostructures via electrospinning. *Prog. Polym. Sci.* **2014**, *39*, 862–890.
33. Darkwah, W.K.; Oswald, K.A. Photocatalytic applications of heterostructure graphitic carbon nitride: Pollutant degradation, hydrogen gas production (water splitting), and CO2 reduction. *Nanoscale Res. Lett.* **2019**, *14*, 234. doi:10.1186/s11671-019-3070-3.